MARINE ROBOTICS

Copyright © 2021 The Authors, some rights reserved; exclusive licensee American Association for the Advancement of Science. No claim to original U.S. Government Works

A system of coordinated autonomous robots for Lagrangian studies of microbes in the oceanic deep chlorophyll maximum

Yanwu Zhang[1]*, John P. Ryan[1], Brett W. Hobson[1], Brian Kieft[1], Anna Romano[2], Benedetto Barone[2], Christina M. Preston[1], Brent Roman[1], Ben-Yair Raanan[1], Douglas Pargett[1], Mathilde Dugenne[2], Angelicque E. White[2], Fernanda Henderikx Freitas[2], Steve Poulos[2], Samuel T. Wilson[2], Edward F. DeLong[2], David M. Karl[2], James M. Birch[1], James G. Bellingham[3], Christopher A. Scholin[1]

The deep chlorophyll maximum (DCM) layer is an ecologically important feature of the open ocean. The DCM cannot be observed using aerial or satellite remote sensing; thus, in situ observations are essential. Further, understanding the responses of microbes to the environmental processes driving their metabolism and interactions requires observing in a reference frame that moves with a plankton population drifting in ocean currents, i.e., Lagrangian. Here, we report the development and application of a system of coordinated robots for studying planktonic biological communities drifting within the ocean. The presented Lagrangian system uses three coordinated autonomous robotic platforms. The focal platform consists of an autonomous underwater vehicle (AUV) fitted with a robotic water sampler. This platform localizes and drifts within a DCM community, periodically acquiring samples while continuously monitoring the local environment. The second platform is an AUV equipped with environmental sensing and acoustic tracking capabilities. This platform characterizes environmental conditions by tracking the focal platform and vertically profiling in its vicinity. The third platform is an autonomous surface vehicle equipped with satellite communications and subsea acoustic tracking capabilities. While also acoustically tracking the focal platform, this vehicle serves as a communication relay that connects the subsea robot to human operators, thereby providing situational awareness and enabling intervention if needed. Deployed in the North Pacific Ocean within the core of a cyclonic eddy, this coordinated system autonomously captured fundamental characteristics of the in situ DCM microbial community in a manner not possible previously.

INTRODUCTION

Robotic applications to scientific studies in the ocean face challenges that are distinct from those in terrestrial robotic settings, particularly with regard to communications, navigation, and fluid motion (*1*, *2*). Communication in the ocean is far more limited because water strongly attenuates electromagnetic radiation (*3*). This necessitates acoustic communication, which is energy intensive, low bandwidth, and typically constrained to spatial scales of several kilometers using commercially available modems (*4*–*6*). Longer-range communication reaching hundreds of kilometers is possible in the SOFAR (sound fixing and ranging) channel (*7*), but this requires use of low-frequency (<1 kHz) sound sources and placement of both transmitter and receiver in the SOFAR channel (*8*). Robotic underwater navigation is prone to error that can be mitigated by periodic ascents to the sea surface for GPS fixes, transmitting sound waves and measuring Doppler frequency shift in echoes when a solid reference surface (seafloor or ice floe) is within range (*9*), or ranging to acoustic beacons at known locations (*10*), but at increased operational complexity and cost. Fluid motions introduce difficulties in navigating robotic platforms where they are needed to effectively measure changes in the oceanic environment and in precisely sampling populations of microscopic life that are moving with the ocean currents.

[1]Monterey Bay Aquarium Research Institute, Moss Landing, CA, USA. [2]University of Hawai'i at Mānoa, Honolulu, HI, USA. [3]Woods Hole Oceanographic Institution, Woods Hole, MA, USA.
*Corresponding author. Email: yzhang@mbari.org

Studies of marine microbiology can use a spatial reference frame that is fixed to the Earth (Eulerian) or moving with ocean circulation (Lagrangian) (*11*). Applications of Eulerian methods are more accessible because the observing system can be moored at a fixed location. Eulerian robotic sampling systems have been used to study a variety of oceanic phenomena in environments from near the surface (*12*) to the deep seafloor (*13*, *14*). In most scientific applications of autonomous underwater vehicles (AUVs), the vehicle transects the ocean to survey a feature of interest (*15*–*17*), so the operational mode is neither Eulerian nor Lagrangian. Applications of Lagrangian methods are more challenging because the system must effectively remain with a targeted fluid patch that moves and changes under the influence of many physical processes (*18*, *19*). However, these methods are essential to understanding the fundamental role microbial communities play in modulating major biogeochemical transformations of global significance (*20*). It is this more challenging domain and the importance of its use that are the focus of this work.

A number of field experiments have used Lagrangian approaches to study physical and biological processes in the ocean. One approach is the use of free-drifting subsurface floats (without surface components). Isobaric SOFAR floats were used to study mesoscale variability in the western North Atlantic (*21*, *22*). Isopycnal RAFOS (SOFAR source/receiver reversed) floats enabled investigation of cross-stream transport and upwelling in the Gulf Stream (*23*). Neutrally buoyant Lagrangian floats were applied to study convection in the Labrador Sea (*24*–*26*) and mesoscale dynamics that influence the North Atlantic spring bloom of phytoplankton (*20*). A phytoplankton patch formation mechanism in an internal wave field was examined

Downloaded from http://robotics.sciencemag.org/ at MLML MBARI on January 13, 2021

using a swarm of depth-holding robotic drifters, with the aid of an array of moored acoustic pingers each with a GPS receiver at the sea surface (*27*).

A second approach to Lagrangian observation uses drifting platforms with surface components to guide ship and AUV sampling. For example, in the equatorial Pacific and Southern Ocean iron enrichment experiments (*28*, *29*), a research vessel followed a drifter that was moving with prevailing currents to study a phytoplankton bloom. The drifter was composed of a drogue deployed in the mixed layer at 15-m depth, tethered to a surface float. Similarly, another study followed in situ diel gene expression in the nitrogen-fixing cyanobacterium *Crocosphaera*, by following a drifter (also drogued at 15-m depth and tethered to a surface float) and collecting water samples using ship-deployed Niskin bottles attached to a conductivity-temperature-depth (CTD) sensor package (*30*). In a study of harmful algal bloom (HAB) ecology in coastal waters, a phytoplankton patch marked by a drogued drifter was tracked and sampled by two AUVs to reveal heightened phytoplankton cellular toxicity, where cells were exposed to seafloor sediment suspended in the water column (*31*).

Lagrangian observation can be augmented by enabling water sampling to occur autonomously aboard a drifting platform. For example, the environmental sample processor (ESP) is a robotic molecular analytical instrument developed to acquire and process water samples for in situ assessment of the presence and abundance of specific organisms, genes, and metabolites, as well as preserve material for subsequent laboratory analyses (*32*, *33*). A second-generation ESP (2G-ESP) suspended beneath a free-drifting surface float was applied toward Lagrangian sampling of shallow (<25 m) microbial populations off the northern California coast and in the North Pacific Subtropical Gyre to reveal microbes' diel cycles and responses to varying biogeochemical conditions (*34*–*37*). This system enabled observations in a moving reference frame; however, it was limited to a single sampling depth, and the drift trajectory was subject to effects of wind and currents on the surface float and tether. These limitations have been overcome through technological advancements in the ESP and the platforms that support its operation and mobility, as described below. To understand the drivers of these robotic advancements, it is necessary to first understand the oceanographic context and the observational challenges it presents.

Oceanographic context

Marine photosynthesis accounts for about half of the global net primary production (*38*, *39*), which supplies atmospheric oxygen, initiates oceanic sequestration of about 30% of anthropogenic carbon dioxide (*40*), and fuels the marine food web. Marine microbial activities play a key role in driving Earth's biogeochemical cycles (*41*). In the pycnocline of the open ocean, at the base of the nutrient-impoverished surface layer (~100-m depth), nutrient concentrations increase and light levels decrease with increasing depth (Fig. 1A). This creates a vertically limited layer in which photosynthetic microbes can access both nutrients from below and light from above. The result is a layer of enhanced chlorophyll concentration, referred to as the deep chlorophyll maximum (DCM) (*42*, *43*). The DCM is a ubiquitous feature of stratified open-ocean ecosystems.

Mesoscale eddies alter the vertical distributions of nutrients and microbial populations in the ocean, thereby influencing ecosystem functioning and global biogeochemical cycles (*44*). Eddies in our study region (north of the Hawaiian Islands) have a mean radius of ~100 km and a median propagation speed of 6.5 cm/s (mostly in the westward direction) (*45*), and they are responsible for about half of the variance in sea level (*45*–*47*). When cyclonic eddies (counterclockwise rotation in the Northern Hemisphere) intensify, the upwelling of nutrient-rich water can stimulate primary production and export of organic matter to the deep sea (*48*, *49*). The uplifted nutricline leads to increased rates of nutrient diffusion at the DCM and generally to an increase in the abundance of photosynthetic picoeukaryotes (PPEs) (*45*). A cyclonic eddy is characterized by a sea-level depression in the eddy core, i.e., a negative sea-level anomaly (SLA). Figure 1 (B and C) shows a cyclonic eddy and the DCM within it as surveyed by two long-range AUVs (LRAUVs) (*50*), named *Aku* and *Opah* (after two charismatic pelagic fishes), on approximately orthogonal cross-eddy transects.

A system approach to Lagrangian observation of the DCM microbial community

The DCM cannot be observed using aerial or satellite remote sensing because it is far below the first optical depth (*51*, *52*) from which most upwelling light available to above-sea remote sensing originates. Therefore, in situ methods of observation are essential. Because populations of microscopic organisms move with prevailing ocean currents, understanding the processes that drive dynamics and metabolism within a microbial community requires observing in the moving reference frame of a community and its local environment. The goal of making continuous observations and collecting discrete samples from within the DCM in a Lagrangian reference frame presents a much greater challenge to robotic sampling systems relative to previous studies because of the relatively deep location of the DCM plankton populations (Fig. 1) and their vertical displacements due to physical perturbations (e.g., internal tides and inertial oscillations). When a ~100-m-depth drogue tethered to a surface float is used to trace the DCM, the drifter's motion is not governed only by the DCM layer velocity; it also integrates the velocities of the shallower layers (due to drag on the surface float and tether), which generally differ from the DCM layer velocity, hence compromising the coherence of Lagrangian observations. In addition, the drogue is set at a fixed depth, whereas the DCM depth is known to move vertically, as much as 36 m within 4 hours (*53*).

Meeting the challenge of Lagrangian DCM observation requires a coordinated system of robotic platforms, each achieving specific tasks (Fig. 2A). The focal platform is tasked with Lagrangian sampling of a DCM population and monitoring of its local environment. These tasks are achieved by integrating a third-generation ESP (3G-ESP) (*33*, *54*) with an LRAUV (*50*, *55*) (*Aku*). *Aku* uses real-time environmental assessments, first, to locate the DCM and, then, to remain within the DCM, following a targeted microbial population that moves horizontally and vertically. While *Aku*'s horizontal motion is governed by drifting with ambient ocean currents, its vertical motion is actively controlled to track the vertical displacements of the DCM. *Aku*'s capabilities precisely position the 3G-ESP to acquire a time series of Lagrangian biological samples. Further, the vehicle frees subsurface sample collection from the vagaries of a surface float connection and crewed ship operations (*33*, *56*).

The observing system integrates two essential coordinated operations (Fig. 2A), monitoring environmental conditions surrounding the tracked microbial community and providing situational awareness. Because environmental sensing from the focal Lagrangian platform is localized to the drifting community, simultaneous measurements

Downloaded from http://robotics.sciencemag.org/ at MLML MBARI on January 13, 2021

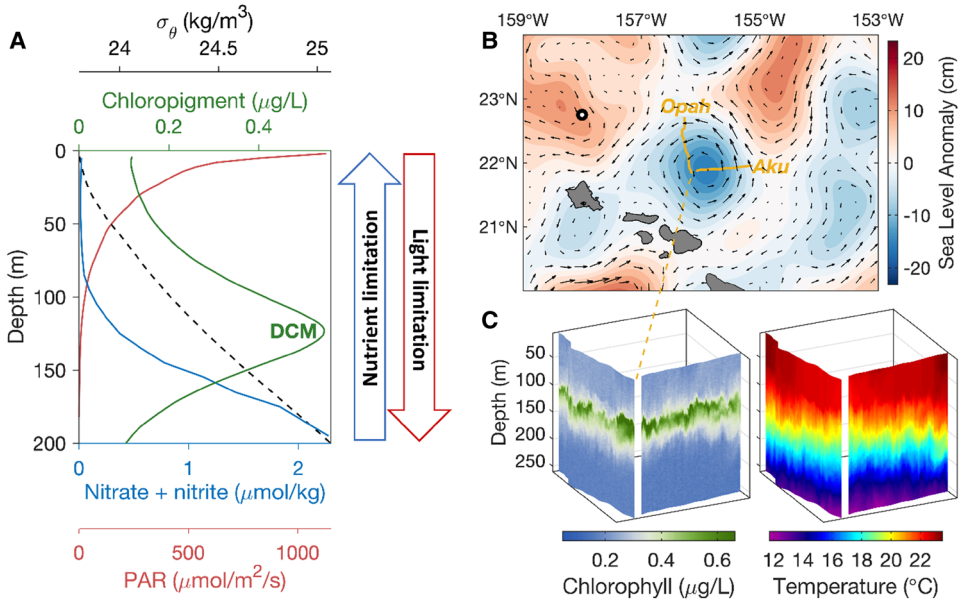

Fig. 1. Water column properties at Station ALOHA and at the experiment site in the eddy. (**A**) Averaged profiles of potential density anomaly (σ_θ; potential density − 1000 kg/m^3), chloropigment (chlorophylls + phaeopigments) concentration, the sum of nitrate and nitrite concentrations, and photosynthetically active radiation (PAR) for March and April at Station ALOHA (22°45′N, 158°W), north of the Hawaiian Islands (see the Supplementary Materials). The center of the DCM is labeled. (**B**) Two 100-km transects (gold solid lines) across a cyclonic eddy north of the Hawaiian Islands (14 to 16 March 2018) by LRAUVs *Aku* and *Opah*, overlaid on an SLA map for 14 March. Arrows represent geostrophic velocities (0 to 0.89 m/s). Station ALOHA is marked by the circle. (**C**) Perspective views of chlorophyll and temperature measured by the two LRAUVs as they ran on sawtooth trajectories on the respective 100-km transects to acquire 274 profiles from near the surface to 250-m depth starting from the eddy's edge and progressing into the eddy interior. The transects were completed in 38 hours (*Aku*) and 35 hours (*Opah*).

within the overlying and underlying water column are required to understand environmental processes influencing community dynamics and metabolism. This is achieved by a second LRAUV (*Opah*) that acoustically tracks (*57*) the focal platform and continuously profiles vertically to measure water column conditions. Situational awareness, required to monitor subsurface operations and intervene if necessary, is achieved by a gateway surface vehicle (*Mola*) that acoustically tracks *Aku*, receives data on *Aku*'s operational status, and converts received acoustic signal into electromagnetic signal that is relayed via satellite and Internet (*58*).

RESULTS

Multirobot sampling and characterization of the DCM in a cyclonic eddy

During the 2018 Simons Collaboration on Ocean Processes and Ecology (SCOPE) Eddy Experiment (*53*, *59*), we deployed the robotic observing system (Fig. 2) north of the Hawaiian Islands. From 17 March to 2 April, the system was situated near the center of a cyclonic eddy. Before the deployment, the eddy center was identified on the basis of satellite SLA maps and ship-measured current velocities and density profiles. Concurrently with the launch of the robotic fleet, a drifter comprising a surface float (with GPS tracking) and a drogue at 120-m depth was deployed as an approximate marker of the DCM layer. The 120-m depth was set to be close to the median depth of the DCM during March and April at Station ALOHA (Fig. 1A) (*60*).

LRAUV *Aku* with a 3G-ESP autonomously tracked and sampled the DCM for several days without surfacing during each of two deployments. Between deployments, the fully expended sampling capacity of *Aku* was renewed. During *Aku*'s submerged sampling missions, LRAUV *Opah* acoustically tracked *Aku* while spiraling up and down near *Aku* to measure spatial and temporal variations in water column properties surrounding points of sample collection (Fig. 2B). Wave Glider *Mola* acoustically tracked *Aku* and relayed its location to R/V *Falkor* (via Iridium satellite communications and Internet), allowing the scientists on the ship to monitor *Aku*'s track in real time, whereas *Opah* surfaced every few hours to transmit environmental data (temperature, salinity, and chlorophyll) for examination by scientists on the ship and on shore.

This experiment comprised two legs. The cyclonic eddy persisted through both legs; however, it weakened over time (Fig. 3A). A stronger cyclonic eddy is associated with a deeper sea-level depression in the eddy core. Between leg 1 and leg 2, sea level in the eddy core shallowed by 1.7 cm (12% change), indicating that the eddy was weakening. This weakening was evident in data from not only satellite remote sensing but also in situ physical and bio-optical measurements. Between the two legs, the upper ocean warmed and the isothermal surfaces deepened (Fig. 3C), and the DCM (Fig. 3D) deepened (from 100 to 105 m on average) and thinned (from 16 to 9 m based on the average vertical distance between chlorophyll isopleths 10% lower than the peak chlorophyll level). The DCM resided in lighter water in leg 2 (fig. S1). The 3G-ESP acquired 64 DCM samples over the two legs, mostly at 3-hour intervals triggered on a timer to study diel cycles (Fig. 3D).

Despite vertical movements of the DCM peak of as much as 36 m in 4 hours, *Aku* accurately and persistently remained within the DCM (Fig. 3D). This was achieved by tracking the isotherm that corresponded to the peak chlorophyll fluorescence in the DCM, identified during an initial profile between the surface and 260-m depth (see Materials and Methods). Autonomous depth control of *Aku* during Lagrangian drifting is illustrated in Fig. 4. The differences between the actual temperature and the targeted temperature (ΔTemperature) remained small throughout the mission (98.4% within ±0.15°C). *Aku* consistently ascended in cool thermal offsets and descended in warm thermal offsets (Fig. 4A), and the magnitude of the AUV depth-rate response was proportional to the magnitude of ΔTemperature (Fig. 4B).

Multiple results indicate that *Aku* was effectively Lagrangian within the DCM. In addition to vertical control maintaining *Aku* within the DCM (Fig. 4), *Aku*'s continuous horizontal motion on a small circle (~10-m radius) integrated to zero net horizontal displacement relative to the targeted DCM community. Ship-based measurements of current velocity near in depth (<4 m) and horizontal distance (<5 km) to the drifting *Aku* (see the Supplementary Materials) confirm effective Lagrangian behavior. *Aku*'s drift velocity was consistent with the ship-measured current velocity in both direction and magnitude

Downloaded from http://robotics.sciencemag.org/ at MLML MBARI on January 13, 2021

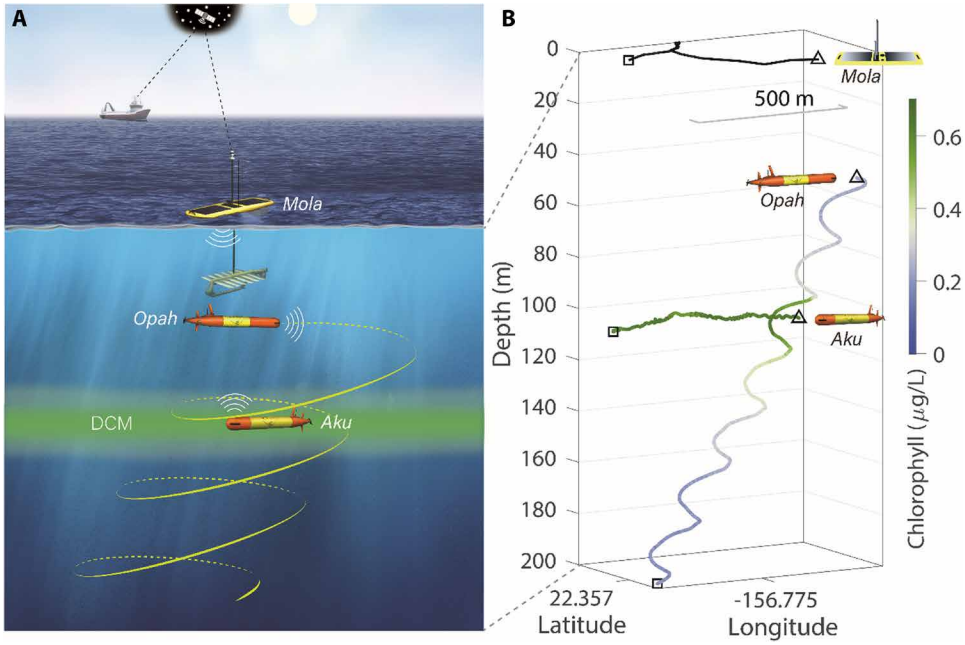

Fig. 2. The system of coordinated autonomous robots. (**A**) Illustration of the coordinated, fully autonomous operation of LRAUVs *Aku* and *Opah*, and Wave Glider *Mola*. (**B**) Tracks of *Aku*, *Opah*, and *Mola* from 31 March 10:03 to 10:40 UTC (from triangle to square). *Aku* was in the process of collecting one sample within the DCM, while *Opah* spiraled downward using *Aku* as the centroid navigational target. The color of the subsurface lines depicts the fluorescence-derived concentration of chlorophyll. *Mola*, on the sea surface (black line), tracked *Aku* and is seen dithering above for a short time as *Aku*'s drift slowed and then accelerated.

(fig. S2). Speed estimates from matched segments of ship acoustic doppler current profiler (ADCP) measurements and *Aku* drift trajectory (fig. S2) were statistically equivalent (see the Supplementary Materials). During both legs, the horizontal trajectory of *Aku*'s drift was similar to that of the drogued drifter, and both platforms' trajectories closely aligned with local geostrophic velocity vectors (*61*) derived from satellite radar altimetry (Fig. 3A). However, the drifter traveled farther in the prevailing currents in each leg (Fig. 3A). This was likely due to the influence of stronger currents between the surface and the 120-m drogue depth than at the DCM depth (fig. S3), which would have acted on the float and tether of the drogued drifter and caused it to move more rapidly than currents at the depth of the DCM itself.

During approximately the first 1.5 days of leg 1, *Opah* did not establish steady acoustic tracking of *Aku*, leading to a relatively large distance between the two vehicles (Fig. 3B) and therefore less accurate contextual sensing. For example, the relatively large spatial separation between *Aku* and *Opah* late on 18 March (Fig. 3B) coincided with an apparent departure of *Aku* from the *Opah*-observed DCM (Fig. 3D). However, *Aku*'s ΔTemperature remained small during this period (97.5% within ±0.15°C), indicating that *Aku* was accurately tracking the DCM. In the later portion of leg 1 and in the entire leg 2, *Opah* established steady acoustic tracking of *Aku*, so the distance between them substantially decreased (Fig. 3B), which supported better description of *Aku*'s contextual water properties in relation to the DCM (Fig. 3, C and D).

Biological data

As *Aku* tracked and sampled the DCM, a CTD rosette was deployed from R/V *Falkor* at a series of stations to collect water samples from within, above, and below the DCM using Niskin bottles. To describe diversity of the 4- to 100-μm-sized nano- and microplankton, particles in these samples were imaged at high resolution (3.2 pixels/μm) using a McLane Imaging FlowCytobot (IFCB) (*62*) onboard R/V *Falkor*. The DCM community (Fig. 5) was predominantly composed of photosynthetic diatoms (e.g., *Chaetoceros*, *Licmophora*, *Corethron*, *Pseudo-nitzschia*, and *Thalassionema*) and coccolithophores (e.g., *Ophiaster*, *Calciopappus*, and *Michaelsarsia*). The DCM community was distinct from the surface community, which was mostly dominated by planktonic grazers, as has been previously observed using traditional light microscopy (*63*).

Biological characterization of the microbial community from water samples uses, among other methods, RNA-based transcriptomics to examine spatial and temporal variations in gene expression. Here, we evaluate sampling effectiveness by examining the quality and amount of RNA recovered from samples. RNA quality number (RQN) provides a metric of RNA integrity and quality, based on the degradation of large subunit (LSU) ribosomal RNA (rRNA) by comparing the relative amounts of LSU rRNA and small subunit (SSU) rRNA detected and quantified during electrophoresis (*64*). Total RNA quantifies the amount of RNA isolated per unit volume of seawater sample.

The 3G-ESP enabled effective sampling of particulate matter within the DCM (Fig. 3), as well as below and above the DCM. RQN and total RNA were measured for 81 ESP samples (64 from the DCM, 10 from 250-m depth, and 7 from 50-m depth), as well as 90 CTD rosette samples (36 from the DCM, 18 from 250-m depth, and 36 from 50-m depth). Unlike samples from the CTD rosette, which were processed and frozen (−80°C) in the shipboard laboratory immediately upon return to the surface, samples from the ESP were preserved onboard *Aku* at ambient oceanic temperature when submerged and then stored at ambient atmospheric temperature on the ship after the vehicle was recovered. After R/V *Falkor* returned to shore, the ESP samples were recovered and frozen until further processing.

ESP sample preservation was effective. Despite in situ oceanic temperature hold times of up to 5 days (17 to 22 March) after leg 1 DCM sampling plus an atmospheric temperature hold time of 1 day (22 to 23 March), ESP samples maintained RQN values that were as high as those for shipboard CTD rosette samples (Fig. 6, A and C). Similarly, despite in situ oceanic temperature hold times up to 6 days (28 March to 3 April) after leg 2 DCM sampling plus an atmospheric temperature hold time of 7 days (3 to 10 April), ESP samples had RQN values of similar magnitude as those for shipboard CTD rosette samples (Fig. 6, B and C). RQN values near and above 7 are generally considered to be high quality and sufficient for preparing complementary DNA samples for sequencing library preparation and subsequent transcriptomic analysis. The high RQN of samples from both sampling approaches (Fig. 6C) provides confidence in

Downloaded from http://robotics.sciencemag.org/ at MLML MBARI on January 13, 2021

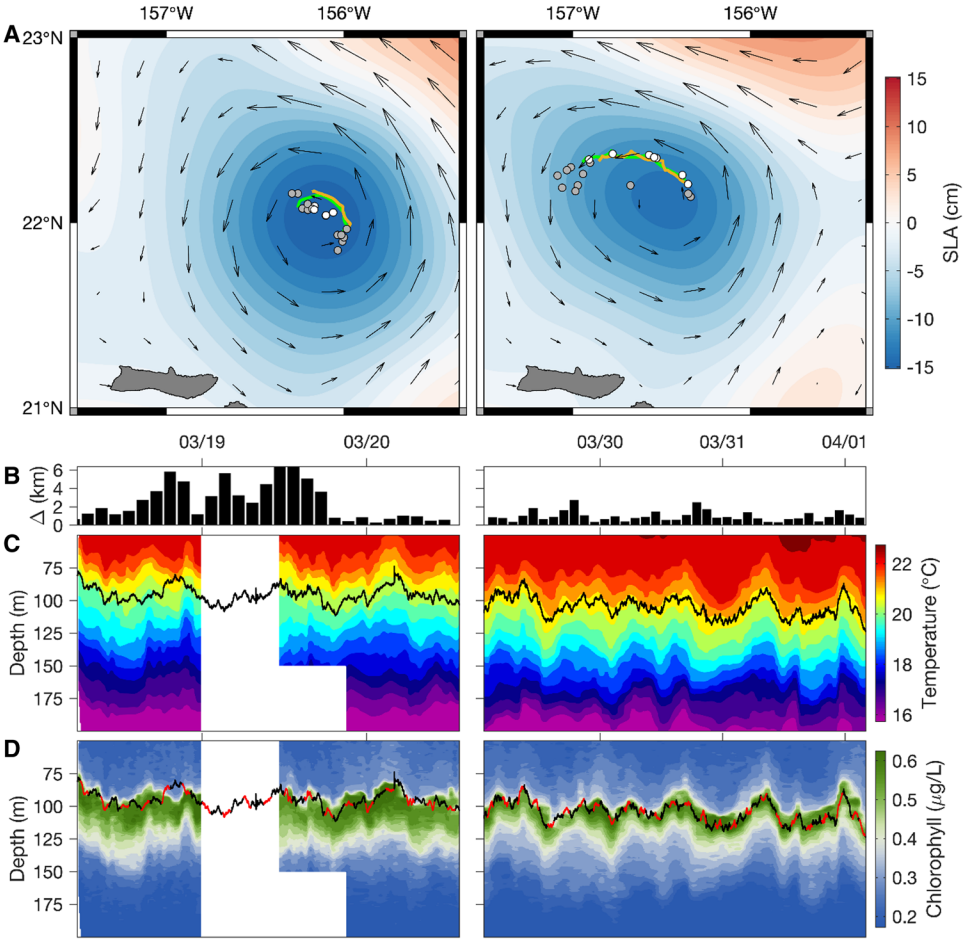

Fig. 3. Trajectories, tracking, and environmental conditions of the Lagrangian drifts. (**A**) Tracks of *Aku* (gold) and the drogued drifter (green) on legs 1 (left) and 2 (right) overlaid on SLA and geostrophic velocity maps averaged for each drift period. Current speed ranges represented by the arrows are 0.01 to 0.45 m/s and 0.01 to 0.49 m/s, respectively. Tracks represent the longest contiguous DCM sampling segment in each leg, both beginning at the eastern side of the eddy. Circles show locations of the DCM samples acquired by the shipboard CTD rosette, during (white) and preceding or following (gray) the *Aku* drift period shown. (**B**) Distance between *Aku* and *Opah*. (**C** and **D**) *Aku*'s time-depth trajectory (black line) overlaid on water column temperature and chlorophyll measured by *Opah*. In (D), ESP sample collection periods are marked red. Time is UTC. On 19 March, water column data were limited because the profiling depth of *Opah* was temporarily reduced (to 50 m in the first half of the day; to 150 m in the second half) in the process of reestablishing acoustic tracking of *Aku*.

the analysis of temporal variation in total RNA in DCM samples, as well as comparison between DCM and shallow (50 m) samples (Fig. 6D). Lower RQN for deep samples (250 m; Fig. 6D) likely resulted from collecting less particulate organic matter, some of which was in the processes of degradation and remineralization.

The measured variations in total RNA provided insight into microbial ecology. The focal temporal dimension is that of eddy weakening, as represented by DCM data grouped within each sampling leg. As indicated by both ESP and shipboard sample results, total RNA in DCM samples decreased between the two sampling legs (Fig. 7C). DCM samples from the two legs were from populations having different distributions of total RNA (by Wilcoxon rank-sum test, $P < 0.01$). The difference between the means from the two legs was nonzero (by Student's t test, $P < 0.01$), with the mean of the leg 1 DCM set being higher. Consistent with total RNA results, concentrations of chloropigment and PPEs (0.8- to 3-μm size) within the layer 75 to 125 m, spanning the DCM (Fig. 3D), were higher during sampling leg 1 (fig. S4). The median chloropigment concentration decreased from 1.00 μg/liter during leg 1 to 0.57 μg/liter during leg 2; the median PPE concentration decreased from 2950 cells/ml during leg 1 to 1626 cells/ml during leg 2. The distributions in the two groups for each variable differed significantly, with leg 1 exhibiting a stochastically higher distribution (by Wilcoxon rank-sum test; $n1 = 46$, $n2 = 15$; $P < 0.001$, one-tailed). Compared with the shipboard DCM samples, ESP DCM samples showed less variation in total RNA and greater overlap between the two sampling legs (Fig. 7, A to C). This is likely due to more precise and consistent acquisition of DCM samples by the LRAUV autonomously tracking the peak chlorophyll isotherm (Figs. 3 and 4), compared with manual triggering of the CTD rosette Niskin bottles at the visually determined peak chlorophyll isotherm defined from the first CTD cast (see the Supplementary Materials).

The focal spatial dimension is vertical—within, below, and above the DCM. Molecular, optical, and cell count data together support that the sampling results from the optically targeted DCM peak represent a local phytoplankton biomass maximum in the cyclonic eddy. Total RNA concentrations from both sampling platforms were highest in DCM samples (Fig. 7D). Comparison of DCM with both 50 and 250 m showed that the sample sets were from populations having different distributions (by Wilcoxon rank-sum test, $P < 0.01$), and the difference between the means was nonzero (by Student's t test, $P < 0.01$). The DCM in the study region is identified by the fluorescence of light-harvesting pigments (Figs. 1 to 3) (*65*). However, the DCM in this region does not always coincide with the maximum particle concentrations in the water column (*66*). Particle concentrations can be described by optical beam attenuation (*67*). During both legs of the study, measurements of chloropigment and particulate beam attenuation coefficient (c_p) showed that the DCM coincided with a local particle concentration maximum (fig. S1). PPE (0.8 to 3 μm) exhibited peak concentrations in the DCM that were more than twice those in the overlying and underlying water column (fig. S4). In addition, concentrations of larger phytoplankton (4 to 100 μm; Fig. 5) were much higher in the DCM (mean ± one SD = 18697 ± 3933 cells/liter) compared with 5 m (7122 ± 1796 cells/liter) and 15 m (9903 ± 3071 cells/liter).

Downloaded from http://robotics.sciencemag.org/ at MLML MBARI on January 13, 2021

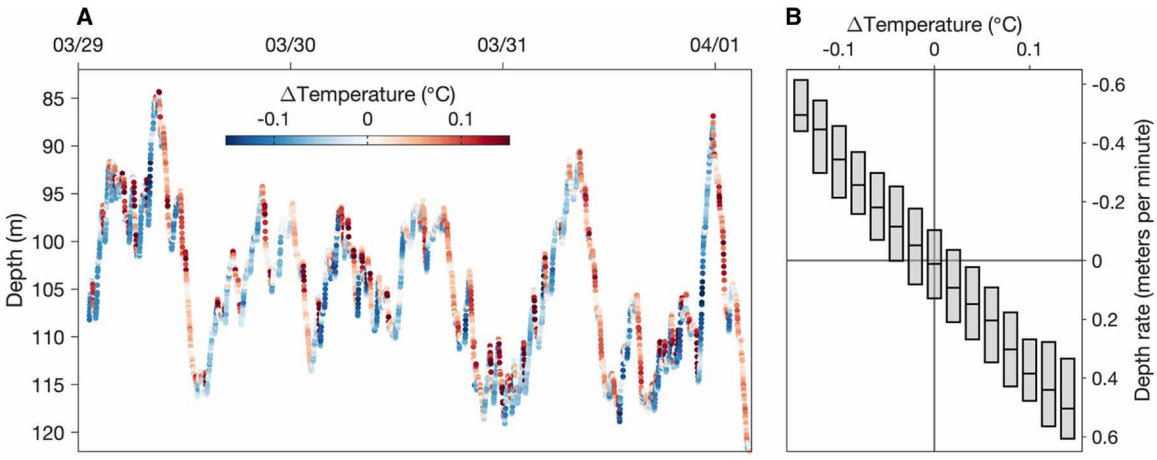

Fig. 4. Autonomous temperature-based depth control. (**A**) Depth of *Aku* during the Lagrangian drift in leg 2, colored by ΔTemperature (actual minus target). (**B**) Statistical summary of *Aku* depth rate in relation to ΔTemperature; boxes show the interquartile range (IQR; 25th to 75th percentiles) and median. Time is UTC.

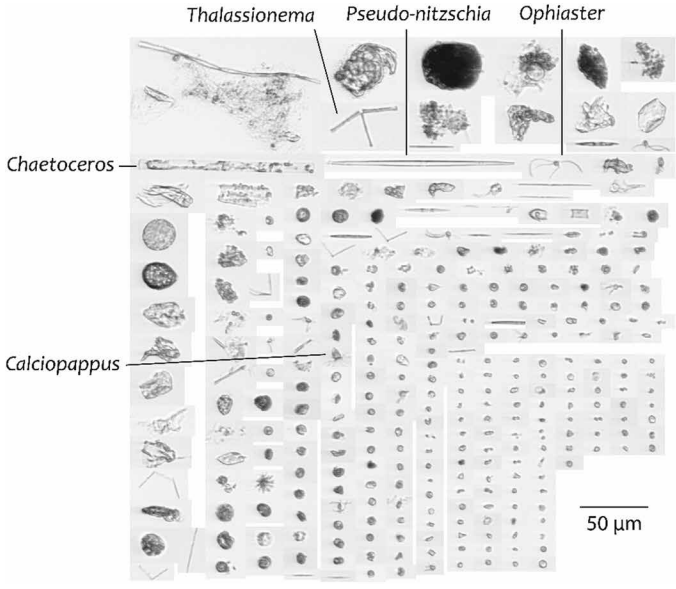

Fig. 5. Microphotographs of organisms in a water sample from the DCM. Images were taken by an Imaging FlowCytobot. Representative phytoplankton species are noted in text for diatoms (*Chaetoceros*, *Thalassionema*, and *Pseudo-nitzschia*) and coccolithophores (*Ophiaster* and *Calciopappus*).

DISCUSSION

Observing in a Lagrangian framework is essential for detecting the response of microbial populations to variable environmental processes that drive their metabolism and interactions. The robotic challenges for achieving this goal included (i) autonomous tracking and sampling of a targeted DCM community that was horizontally drifting and vertically moving, (ii) autonomous sampling and effective preservation of suspended particles and nucleic acids onboard an underwater robot, (iii) autonomous contextual characterization of the environment around the sampling robot, and (iv) real-time tracking of subsea robots. To address these challenges, we developed a system comprising three robotic platforms, one of which contained a robotic sampler. The focal platform integrated autonomous feature recognition and localization, sample acquisition, and sample preservation onboard an LRAUV that tracked and sampled the DCM in an open-ocean eddy. Acoustically coordinated multivehicle operations enabled an environmental sensing LRAUV to track the sampling LRAUV and provide contextual ecosystem data and a gateway surface vehicle to track the sampling LRAUV for situational awareness. Collectively, this coordinated robotic system autonomously captured changes of the DCM microbial community in its natural frame of reference as it moved with ocean currents, and it enabled comparison of DCM populations with those shallower and deeper in the water column.

Successful preservation of RNA in the 3G-ESP samples onboard the LRAUV over extended durations is a requirement for accurately quantifying variation in microbial transcriptional activities. In this experiment, the 3G-ESP samples consistently showed high RNA quality in samples stored onboard at ambient oceanic and atmospheric temperatures before laboratory processing, for up to 6 days during leg 1 and 13 days during leg 2. Further, the RNA quality of the 3G-ESP samples was similar to that of immediately processed and frozen ship-based rosette samples from both the DCM and 50-m depth. The RNA quality of the 250-m samples was lower than that of the DCM and 50-m samples from both sampling platforms, which was likely due to the low biomass in the deeper samples and the processes of degradation and remineralization acting on sinking and dead phytoplankton-derived particulate organic matter at that depth.

The total RNA data reveal patterns relevant to microbial ecology. While the eddy weakened from leg 1 to leg 2, as described consistently by satellite altimetry and in situ hydrographic data, total RNA in the DCM samples decreased. The RNA quality was sufficiently high to be certain of this temporal change. The decrease in total RNA was consistent with observed decreases in median concentrations of chloropigment (43%) and PPE (45%). These biological changes in the DCM were not likely due to differences in horizontal positioning within the eddy because both drifts began at approximately the same distance from the eddy core and closely followed local geostrophic current vectors. They were unlikely to have been caused by differences in vertical positioning because *Aku* accurately tracked the DCM in the vertical dimension during both legs. The

Downloaded from http://robotics.sciencemag.org/ at MLML MBARI on January 13, 2021

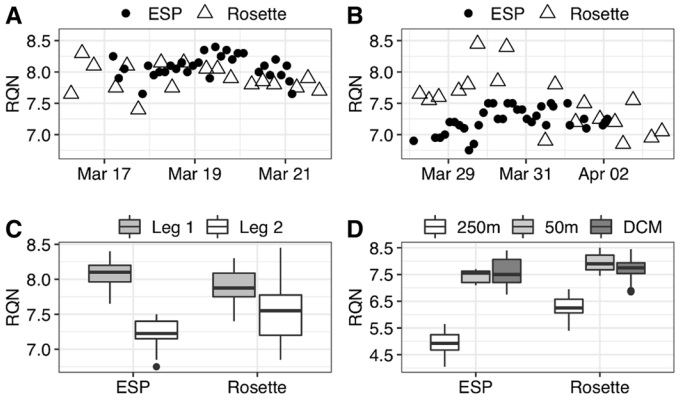

Fig. 6. Sample RNA quality assessment. RQN data are from 0.22- to 5-μm size fraction samples acquired by ESP and CTD rosette sampling platforms. (**A** and **B**) Time series from DCM samples during sampling legs 1 and 2. (**C**) Nonparametric box plots of DCM samples grouped by sampling leg and sampling platform. (**D**) Nonparametric box plots grouped by depth and sampling platform. In (C) and (D), the thick line corresponds to the median; the box spans the IQR; vertical lines extend at most 1.5 × IQR from the first and third quartiles; and data points beyond this range are individually plotted (circles).

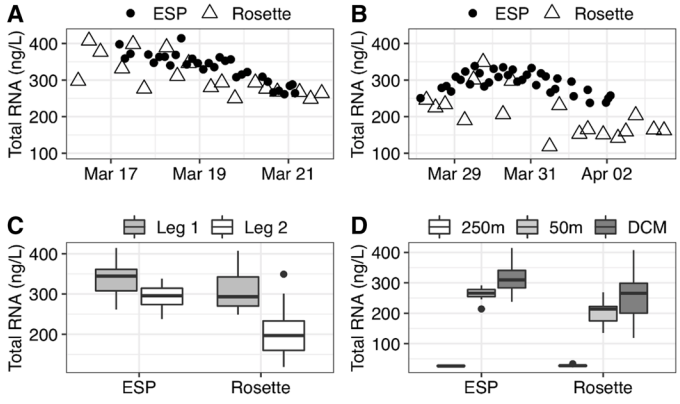

Fig. 7. Sample RNA quantification. Total RNA data are from 0.22- to 5-μm size fraction samples acquired by ESP and CTD rosette sampling platforms. (**A** and **B**) Time series from DCM samples during sampling legs 1 and 2. (**C**) Nonparametric box plots of DCM samples grouped by sampling leg and sampling platform. (**D**) Nonparametric box plots grouped by depth and sampling platform. In (C) and (D), the thick line corresponds to the median; the box spans the IQR; vertical lines extend at most 1.5 × IQR from the first and third quartiles; and data points beyond this range are individually plotted (circles).

changes were also not likely due to differences in incident sunlight, as can result from differences in cloud cover, because sea-surface photosynthetically active radiation (PAR) levels measured during the DCM sampling periods of the two legs were statistically equivalent (see the Supplementary Materials). Therefore, the primary temporal variation in DCM RNA, chloropigment, and PPE concentrations may be explained by biological consequences of the weakening eddy. Specifically, a weaker cyclonic eddy during leg 2 would be associated with weaker uplift of thermocline isopycnals and a lower diapycnal flux of inorganic nutrients at the DCM (*45*), consistent with the observed deepening of the thermocline and deepening and thinning of the DCM layer between the two sampling legs. Transcriptomic analyses of the recovered RNA (now underway) will provide more detailed information on the relationships among spatial and temporal environmental variabilities, microbial community taxonomic composition, and transcriptional activities in the DCM (*30*, *34*, *36*, *37*).

The coordinated robotic system enabled study of a complex global oceanographic phenomenon more efficiently and effectively than possible previously. Ship operations were required to demonstrate the system and compare with traditional ship-based methods. However, advancing capabilities of the autonomous robotic system are intended ultimately to supplant a strict dependence on ship-based research methods, reduce operational costs, and enhance the effectiveness of microbial ecology research. All platforms in the robotic system are capable of long-duration operations, enabling transit to and from the experiment site, such that research can be effectively conducted from shore through electromagnetic (above ocean) and acoustic (in ocean) communication channels.

Ongoing developments will further enhance the effectiveness of robotic ocean observing systems. One development is intervehicle acoustic messaging to improve collaborative operations. By exchanging complementary information across different ecosystem features, the collaborating LRAUVs will be able to make timely adaptations of survey paths and behaviors to identify and concentrate on the most valuable targets. For example, when the sampling LRAUV senses a sharp rise or fall of the DCM depth, it can inform contextual LRAUV(s) to focus around the DCM, thereby enabling better understanding of the physical perturbations that drive DCM depth displacements and corresponding ecological responses. Alternatively, the contextual LRAUV may horizontally localize the strongest optical signal of a biological patch and guide molecular sensing capabilities onboard other LRAUVs to that focal feature.

A second key development is real-time molecular detection. This capability has been applied using 2G-ESP networks to inform human-in-the-loop replanning. For example, real-time data from moored 2G-ESPs guided the deployment strategy for ship and AUV sampling in a study revealing causality of a severely toxic HAB in the Northeast Pacific (*68*). Beyond sample filtration and preservation, the ability to analyze samples onboard mobile 3G-ESPs will enable response to a broader spectrum of ecological processes in near real-time. Microorganisms essential to key biogeochemical or ecological processes often require specific environmental conditions to grow or become active, yet biological processes cannot necessarily be predicted by environmental indicators alone. Real-time molecular results can identify biological events and thereby inform expenditure of limited onboard sampling resources and optimization of coordination within the robotic fleet. Mission adaptation may be autonomously controlled in situ, or it may engage human-in-the-loop replanning through transmission of molecular analytical results through acoustic and satellite communication gateways. These capabilities are initially being developed and tested for detection of HAB toxin in coastal ecosystems (*69*), which can be used to identify, localize, and study HAB hotspots. Augmenting real-time environmental data with real-time molecular data, by expanding onboard 3G-ESP analytical capabilities, will enhance applications of adaptive sampling to a variety of ecosystems and phenomena (*33*).

Downloaded from http://robotics.sciencemag.org/ at MLML MBARI on January 13, 2021

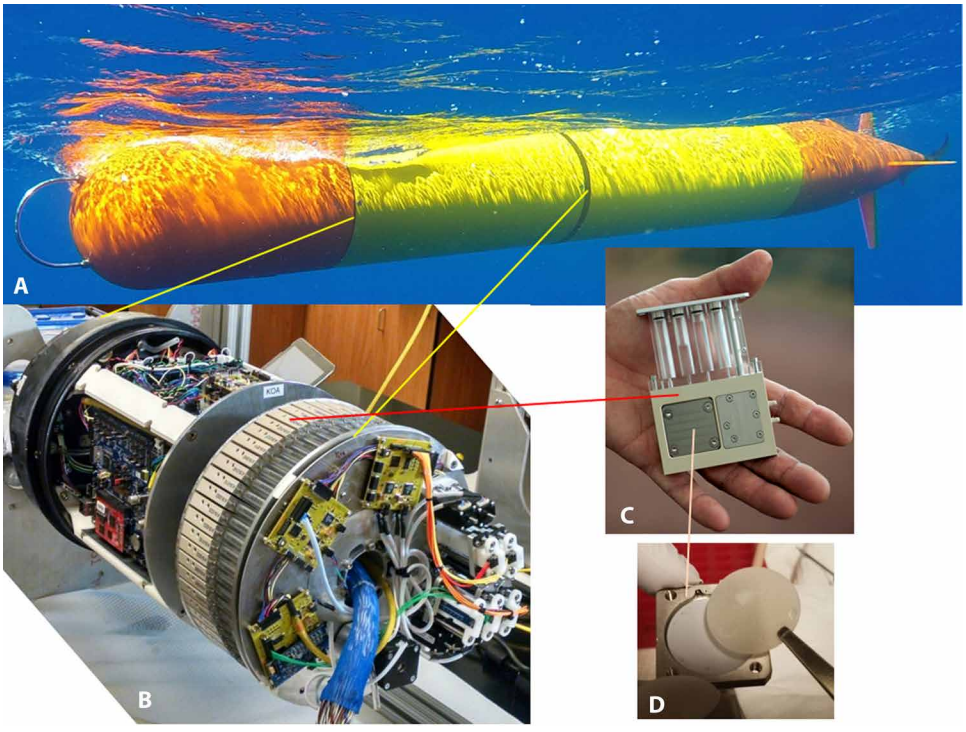

Fig. 8. The robotic sampling vehicle. (**A**) LRAUV *Aku* deployed in March and April 2018 during the SCOPE Eddy Experiment. (**B**) The 3G-ESP installed in *Aku*'s fore-mid section. (**C**) One ESP sample collection cartridge. (**D**) Particulate material on the filter in one ESP cartridge after *Aku*'s recovery. Photo credits: Elisha Wood-Charlson (A, B, and D) and Todd Walsh (C).

MATERIALS AND METHODS

Long-range AUVs

An LRAUV combines the mobility and speed of propeller-driven vehicles with energy savings of buoyancy-driven vehicles (*50*, *55*). The vehicle is 3.2 m long and 0.3 m in diameter at the midsection and uses a pair of elevators for vertical control at high speed (at or near 1 m/s). The LRAUV software architecture uses state configured layered control (*70*), which divides the vehicle's operations into a group of behaviors assigned with hierarchical levels of priority. The vehicle runs a mission script that invokes appropriate behaviors to achieve a specified goal (*50*, *71*). LRAUVs *Aku* and *Opah* carried a suite of sensors to measure water temperature, conductivity, pressure, dissolved oxygen, chlorophyll fluorescence, optical backscatter, and PAR. The chlorophyll concentration is derived from the measured fluorescence based on factory calibration.

Third-generation ESP

The LRAUV *Aku* equipped with a 3G-ESP is shown in Fig. 8. The 3G-ESP (*33*, *54*) is installed in a pressure housing in the midsection of *Aku*. It uses cartridges to filter water samples and preserve the material retained for molecular analysis. Up to 60 cartridges are available for a single deployment, and each cartridge contains the filters and reagents necessary for collecting and processing one sample. The cartridges connect to a central ring of valves that are part of a pumped seawater loop. When the LRAUV mission program triggers a sampling event, the 3G-ESP rotates the motor-driven cartridge wheel to align a designated cartridge with the processing station, where power and actuators can be applied to the cartridge. The pumped seawater loop is rinsed with local sample water, and then actuators open valves to direct the seawater through the cartridge, concentrating particles onto the filters. Water sampling is terminated after reaching a specified filtration volume, time, or rate, and the filtration volume is recorded. Then, the seawater valves are closed and a valve in the cartridge is moved, so the collected particulate material can be processed with reagents to preserve the cellular material for later analysis in the laboratory or to extract an analyte from the sample for real-time detection and quantification (*33*). In this experiment, all particulate samples were preserved with RNAlater (Ambion Inc., Austin, TX) for subsequent analysis in a shoreside laboratory [(*56*); Supplementary Materials]. Each cartridge contained a stack of filters (MilliporeSigma, Burlington, MA) of three different pore sizes—5 μm over 0.22 μm with a backing filter of 0.45 μm—and we analyzed the 0.22- to 5-μm size fraction for RNA quality and quantity. The 0.22- and 5-μm filters are polyvinylidene fluoride membranes, and the 0.45-μm filters are mixed cellulose ester membranes. The ESP filtered about 1.6 liters of seawater in 1 hour for each sample.

LRAUV algorithm for autonomously finding, tracking, and sampling the DCM layer

Autonomous tracking of the DCM was a challenge because the DCM layer moves in depth due to internal tides and inertial oscillations, with vertical excursions of as much as 36 m in 4 hours (*53*). The DCM layer follows an isopycnal (*65*, *72*). When density variation is dominated by temperature variation, an isopycnal can be effectively followed by tracking an isotherm. On the basis of this oceanographic understanding, we designed an algorithm for the LRAUV to autonomously find, track, and sample the DCM layer by tracking the isotherm corresponding to the chlorophyll peak (*53*) (fig. S5): (i) *Aku* descended from the surface to a deep bound of 260 m that was sufficiently deeper than the anticipated DCM depth. On the descent, *Aku* recorded the peak of the chlorophyll signal and the corresponding temperature. (ii) Once it reached the 260-m-deep bound, *Aku* turned to an ascent. (iii) On the ascent, when *Aku* reached the recorded temperature of the chlorophyll peak, it stopped ascending and thereafter actively adjusted its depth to remain at that temperature so as to track the DCM (Fig. 4). To place DCM biological results within the context of the upper water column, *Aku* transitioned to a new sampling mode following the Lagrangian DCM sampling of each leg. This mode involved sequential sampling within, below (at 250-m depth), and above (at 50-m depth) the DCM.

Method for underwater tracking between robots

LRAUV *Opah* and Wave Glider (Liquid Robotics, Sunnyvale, CA) *Mola* both tracked the sampling LRAUV *Aku* using acoustics. *Mola*, *Opah*, and *Aku* were each equipped with a Teledyne Benthos (North Falmouth, MA) directional acoustic transponder that integrates

Downloaded from http://robotics.sciencemag.org/ at MLML MBARI on January 13, 2021

an acoustic modem and an ultra-short baseline acoustic positioning system (*57*). The onboard tracking algorithm contains outlier rejection and low-pass filtering of raw navigation measurements (*73*).

Methods for RNA quality check and quantification

RNA quality was measured using the Fragment Analyzer (AATI, Ames, IA) installed with a 12-capillary 33-cm array. A total of 2 μl of each sample was denatured and prepared with Fragment Analyzer High Sensitivity RNA reagents (DNF-472, AATI) as recommended by the manufacturer. Ribosomal peaks were autoidentified by Prosize 2.0 software, and samples were aligned and referenced against a high-sensitivity RNA ladder run with every 11 samples.

RNA quantification was performed with RiboGreen (Invitrogen, Carlsbad, CA) assay according to the manufacturer's protocol. Samples were diluted 1:5 with nuclease-free water before quantification, performed in technical triplicates, and calculated with RiboGreen's low-range standard curve.

Methods for statistical analysis of RNA data

To examine RQN and total RNA from ESP and shipboard samples, statistical analyses were applied to compare temporally and spatially grouped datasets. All comparisons used the nonparametric Wilcoxon rank-sum test. Some comparisons additionally used the parametric *t* test, if normality was indicated by the Shapiro-Wilk normality test. Equivalence of means was tested using Student's *t* test if equal variances were indicated or Welch's *t* test if unequal variances were indicated, based on the result of Bartlett's test of homogeneity of variances (*74*). We used software R (release 3.5.3; http://R-project.org/) for statistical analysis and plotting.

SUPPLEMENTARY MATERIALS

robotics.sciencemag.org/cgi/content/full/6/50/eabb9138/DC1
Section S1. Method for computing average profiles of physical, chemical, and bio-optical conditions at Station ALOHA.
Section S2. Method for computing statistical summaries from profiles of chloropigment and particulate beam attenuation coefficient from shipboard CTD rosette measurements.
Section S3. Methods for ship-based current velocity measurement and comparison with drift velocities.
Section S4. Methods for shipboard sampling for RNA analysis.
Section S5. Methods for RNA extraction from shipboard and ESP samples.
Section S6. Methods for shipboard sampling for conventional and imaging flow cytometry and statistical analysis.
Section S7. Methods for sea-surface PAR measurement and statistical analysis.
Fig. S1. Ship-based characterization of the DCM.
Fig. S2. Lagrangian drift velocities.
Fig. S3. Vertical variation of horizontal current speed.
Fig. S4. Water-column biomass characterization.
Fig. S5. Localization of the DCM followed by Lagrangian drift within the DCM.
References (*75*, *76*)

REFERENCES AND NOTES

1. L. Whitcomb, D. R. Yoerger, H. Singh, J. Howland, Advances in underwater robot vehicles for deep ocean exploration: Navigation, control, and survey operations, in *Robotics Research* (Springer, 2000), pp. 439–448.
2. J. G. Bellingham, K. Rajan, Robotics in remote and hostile environments. *Science* **318**, 1098–1102 (2007).
3. H. D. Young, R. A. Freedman, *University Physics with Modern Physics* (Pearson, 2016).
4. M. Stojanovic, P.-P. J. Beaujean, Acoustic communication, in *Springer Handbook of Ocean Engineering* (Cham, 2016), pp. 359–386.
5. D. B. Kilfoyle, A. B. Baggeroer, The state of the art in underwater acoustic telemetry. *IEEE J. Ocean. Eng.* **25**, 4–27 (2000).
6. S. Singh, S. E. Webster, L. Freitag, L. L. Whitcomb, K. Ball, J. Bailey, C. Taylor, Acoustic communication performance of the WHOI micro-modem in sea trials of the Nereus vehicle to 11000 m depth, in *OCEANS 2009* (IEEE, 2009).
7. R. J. Urick, *Principles of Underwater Sound* (McGraw Hill Inc., ed. 3, 1983), pp. 159–163.
8. L. Freitag, K. Ball, J. Partan, P. Koski, S. Singh, Long range acoustic communications and navigation in the Arctic, in *OCEANS 2015—MTS/IEEE Washington* (IEEE, 2015), pp. 1–5.
9. D. R. Yoerger, M. Jakuba, A. M. Bradley, B. Bingham, Techniques for deep sea near bottom survey using an autonomous underwater vehicle. *Int. J. Rob. Res.* **26**, 41–54 (2007).
10. J. J. Leonard, A. Bahr, Autonomous underwater vehicle navigation, in *Springer Handbook of Ocean Engineering* (Cham, 2016), pp. 341–358.
11. W. J. Emery, R. E. Thomson, *Data Analysis Methods in Physical Oceanography* (Elsevier, ed. 2, 2001).
12. J. Ryan, D. Greenfield, R. Marin III, C. Preston, B. Roman, S. Jensen, D. Pargett, J. Birch, C. Mikulski, G. Doucette, C. Scholin, Harmful phytoplankton ecology studies using an autonomous molecular analytical and ocean observing network. *Limnol. Oceanogr.* **56**, 1255–1272 (2011).
13. C. D. Taylor, K. W. Doherty, Submersible Incubation Device (SID), autonomous instrumentation for the *in situ* measurement of primary production and other microbial rate processes. *Deep Sea Res. Part I Oceanogr. Res. Pap.* **37**, 343–358 (1990).
14. H. C. Olins, D. R. Rogers, C. Preston, W. Ussler III, D. Pargett, S. Jensen, B. Roman, J. M. Birch, C. A. Scholin, M. F. Haroon, P. R. Girguis, Co-registered geochemistry and metatranscriptomics reveal unexpected distributions of microbial activity within a hydrothermal vent field. *Front. Microbiol.* **8**, 1042 (2017).
15. R. Camilli, C. M. Reddy, D. R. Yoerger, B. A. S. Van Mooy, M. V. Jakuba, J. C. Kinsey, C. P. McIntyre, S. P. Sylva, J. V. Maloney, Tracking hydrocarbon plume transport and biodegradation at Deepwater Horizon. *Science* **330**, 201–204 (2010).
16. Y. Zhang, J. G. Bellingham, J. P. Ryan, B. Kieft, M. J. Stanway, Autonomous four-dimensional mapping and tracking of a coastal upwelling front by an autonomous underwater vehicle. *J. Field Robot.* **33**, 67–81 (2016).
17. T. O. Fossum, G. M. Fragoso, E. J. Davies, J. E. Ullgren, R. Mendes, G. Johnsen, I. Ellingsen, J. Eidsvik, M. Ludvigsen, K. Rajan, Toward adaptive robotic sampling of phytoplankton in the coastal ocean. *Sci. Robot.* **4**, eaav3041 (2019).
18. R. E. Davis, Lagrangian ocean studies. *Annu. Rev. Fluid Mech.* **23**, 43–64 (1991).
19. M. J. Perry, D. L. Rudnick, Observing the ocean with autonomous and Lagrangian platforms and sensors: The role of ALPS in sustained ocean observing systems. *Oceanography* **16**, 31–36 (2003).
20. A. Mahadevan, E. D'Asaro, C. Lee, M. J. Perry, Eddy-driven stratification initiates North Atlantic spring phytoplankton blooms. *Science* **337**, 54–58 (2012).
21. S. C. Riser, The quasi-Lagrangian nature of SOFAR floats. *Deep Sea Res. Part I Oceanogr. Res. Pap.* **29**, 1587–1602 (1982).
22. S. C. Riser, T. H. Rossby, Quasi-Lagrangian structure and variability of the subtropical western North Atlantic circulation. *J. Mar. Res.* **41**, 127–162 (1983).
23. A. S. Bower, T. Rossby, Evidence of cross-frontal exchange processes in the Gulf Stream based on isopycnal RAFOS float data. *J. Phys. Oceanogr.* **19**, 1177–1190 (1989).
24. E. A. D'Asaro, D. M. Farmer, J. T. Osse, G. T. Dairiki, A Lagrangian float. *J. Atmos. Oceanic Tech.* **13**, 1230–1246 (1996).
25. E. A. D'Asaro, Performance of autonomous Lagrangian floats. *J. Atmos. Oceanic Tech.* **20**, 896–911 (2003).
26. E. L. Steffen, E. A. D'Asaro, Deep convection in the Labrador Sea as observed by Lagrangian floats. *J. Phys. Oceanogr.* **32**, 475–492 (2002).
27. J. S. Jaffe, P. J. S. Franks, P. L. D. Roberts, D. Mirza, C. Schurgers, R. Kastner, A. Boch, A swarm of autonomous miniature underwater robot drifters for exploring submesoscale ocean dynamics. *Nat. Commun.* **8**, 14189 (2017).
28. K. H. Coale, K. S. Johnson, S. E. Fitzwater, R. M. Gordon, S. Tanner, F. P. Chavez, L. Ferioli, C. Sakamoto, P. Rogers, F. Millero, P. Steinberg, P. Nightingale, D. Cooper, W. P. Cochlan, M. R. Landry, J. Constantinou, G. Rollwagen, A. Trasvina, R. Kudela, A massive phytoplankton bloom induced by an ecosystem-scale iron fertilization experiment in the equatorial Pacific Ocean. *Nature* **383**, 495–501 (1996).
29. K. H. Coale, K. S. Johnson, F. P. Chavez, K. O. Buesseler, R. T. Barber, M. A. Brzezinski, W. P. Cochlan, F. J. Millero, P. G. Falkowski, J. E. Bauer, R. H. Wanninkhof, R. M. Kudela, M. A. Altabet, B. E. Hales, T. Takahashi, M. R. Landry, R. R. Bidigare, X. Wang, Z. Chase, P. G. Strutton, G. E. Friederich, M. Y. Gorbunov, V. P. Lance, A. K. Hilting, M. R. Hiscock, M. Demarest, W. T. Hiscock, K. F. Sullivan, S. J. Tanner, R. M. Gordon, C. N. Hunter, V. A. Elrod, S. E. Fitzwater, J. L. Jones, S. Tozzi, M. Koblizek, A. E. Roberts, J. Herndon, J. Brewster, N. Ladizinsky, G. Smith, D. Cooper, D. Timothy, S. L. Brown, K. E. Selph, C. C. Sheridan, B. S. Twining, Z. I. Johnson, Southern Ocean iron enrichment experiment: Carbon cycling in high- and low-Si waters. *Science* **304**, 408–414 (2004).
30. S. T. Wilson, F. O. Aylward, F. Ribalet, B. Barone, J. R. Casey, P. E. Connell, J. M. Eppley, S. Ferrón, J. N. Fitzsimmons, C. T. Hayes, A. E. Romano, K. A. Turk-Kubo, A. Vislova, E. V. Armbrust, D. A. Caron, M. J. Church, J. P. Zehr, D. M. Karl, E. F. DeLong, Coordinated regulation of growth, activity and transcription in natural populations

Downloaded from http://robotics.sciencemag.org/ at MLML MBARI on January 13, 2021

of the unicellular nitrogen-fixing cyanobacterium *crocosphaera*. *Nat. Microbiol.* **2**, 17118 (2017).
31. J. P. Ryan, M. A. McManus, R. M. Kudela, M. Lara Artigas, J. G. Bellingham, F. P. Chavez, G. Doucette, D. Foley, M. Godin, J. B. J. Harvey, R. Marin III, M. Messie, C. Mikulski, T. Pennington, F. Py, K. Rajan, I. Shulman, Z. Wang, Y. Zhang, Boundary Influences on HAB phytoplankton ecology in a stratification-enhanced upwelling shadow. *Deep Sea Res. Part II Top. Stud. Oceanogr.* **101**, 63–79 (2014).
32. C. A. Scholin, Ecogenomic sensors, in *Encyclopedia of Biodiversity* (Academic Press, 2013), pp. 690–700.
33. C. A. Scholin, J. Birch, S. Jensen, R. Marin III, E. Massion, D. Pargett, C. Preston, B. Roman, W. Ussler III, The quest to develop ecogenomic sensors: A 25-year history of the Environmental Sample Processor (ESP) as a case study. *Oceanography* **30**, 100–113 (2017).
34. E. A. Ottesen, C. R. Young, J. M. Eppley, J. P. Ryan, F. P. Chavez, C. A. Scholin, E. F. DeLong, Pattern and synchrony of gene expression among sympatric marine microbial populations. *Proc. Natl. Acad. Sci. U.S.A.* **110**, E488–E497 (2013).
35. J. C. Robidart, M. J. Church, J. P. Ryan, F. Ascani, S. T. Wilson, D. Bombar, R. Marin III, K. J. Richards, D. M. Karl, C. A. Scholin, J. P. Zehr, Ecogenomic sensor reveals controls on N_2-fixing microorganisms in the North Pacific Ocean. *ISME J.* **8**, 1175–1185 (2014).
36. F. O. Aylward, J. M. Eppley, J. M. Smith, F. P. Chavez, C. A. Scholin, E. F. DeLong, Ocean basin-wide community transcriptome dynamics are conserved among microbial plankton spanning all three domains of life. *Proc. Natl. Acad. Sci. U.S.A.* **112**, 5433–5448 (2015).
37. B. C. Kolody, J. P. McCrow, L. Zeigler Allen, F. O. Aylward, K. M. Fontanez, A. Moustafa, M. Moniruzzaman, F. P. Chavez, C. A. Scholin, E. E. Allen, A. Z. Worden, E. F. DeLong, A. E. Allen, Diel transcriptional response of a California Current plankton microbiome to light, low iron, and enduring viral infection. *ISME J.* **13**, 2817–2833 (2019).
38. C. B. Field, M. J. Behrenfeld, J. T. Randerson, P. Falkowski, Primary production of the biosphere: Integrating terrestrial and oceanic components. *Science* **281**, 237–240 (1998).
39. M. J. Behrenfeld, J. T. Randerson, C. R. McClain, G. C. Feldman, S. O. Los, C. J. Tucker, P. G. Falkowski, C. B. Field, R. Frouin, W. E. Esaias, D. D. Kolber, N. H. Pollack, Biospheric primary production during an ENSO transition. *Science* **291**, 2594–2597 (2001).
40. N. Gruber, D. Clement, B. R. Carter, R. A. Feely, S. van Heuven, M. Hoppema, M. Ishii, R. M. Key, A. Kozyr, S. K. Lauvset, C. L. Monaco, J. T. Mathis, A. Murata, A. Olsen, F. F. Perez, C. L. Sabine, T. Tanhua, R. Wanninkhof, The oceanic sink for anthropogenic CO_2 from 1994 to 2007. *Science* **363**, 1193–1199 (2019).
41. P. G. Falkowski, T. Fenchel, E. F. DeLong, The microbial engines that drive Earth's biogeochemical cycles. *Science* **320**, 1034–1039 (2008).
42. J. J. Cullen, Subsurface chlorophyll maximum layers: Enduring enigma or mystery solved? *Ann. Rev. Mar. Sci.* **7**, 207–239 (2015).
43. J. Huisman, N. N. Pham Thi, D. M. Karl, B. Sommeijer, Reduced mixing generates oscillations and chaos in the oceanic deep chlorophyll maximum. *Nature* **439**, 322–325 (2006).
44. D. J. McGillicuddy Jr., Mechanisms of physical-biological-biogeochemical interaction at the oceanic mesoscale. *Ann. Rev. Mar. Sci.* **8**, 125–159 (2016).
45. B. Barone, A. R. Coenen, S. J. Beckett, D. J. McGillicuddy, J. S. Weitz, D. M. Karl, The ecological and biogeochemical state of the North Pacific Subtropical Gyre is linked to sea surface height. *J. Mar. Res.* **77**, 215–245 (2019).
46. D. B. Chelton, M. G. Schlax, R. M. Samelson, R. A. de Szoeke, Global observations of large oceanic eddies. *Geophys. Res. Lett.* **34**, L15606 (2007).
47. D. B. Chelton, M. G. Schlax, R. M. Samelson, Global observations of nonlinear mesoscale eddies. *Prog. Oceanogr.* **91**, 167–216 (2011).
48. R. D. Vaillancourt, J. Marra, M. P. Seki, M. L. Parsons, R. R. Bidigare, Impact of a cyclonic eddy on phytoplankton community structure and photosynthetic competency in the subtropical North Pacific Ocean. *Deep Sea Res. Part I Oceanogr. Res. Pap.* **50**, 829–847 (2003).
49. S. L. Brown, M. R. Landry, K. E. Selph, E. J. Yang, Y. M. Rii, R. R. Bidigare, Diatoms in the desert: Plankton community response to a mesoscale eddy in the subtropical North Pacific. *Deep Sea Res. Part II Top. Stud. Oceanogr.* **55**, 1321–1333 (2008).
50. B. W. Hobson, J. G. Bellingham, B. Kieft, R. McEwen, M. Godin, Y. Zhang, Tethys-class long range AUVs—Extending the endurance of propeller-driven cruising AUVs from days to weeks, in *2012 IEEE/OES Autonomous Underwater Vehicles (AUV)* (IEEE, 2012), pp. 1–8.
51. R. M. Letelier, D. M. Karl, M. R. Abbott, R. R. Bidigare, Light driven seasonal patterns of chlorophyll and nitrate in the lower euphotic zone of the North Pacific Subtropical Gyre. *Limnol. Oceanogr.* **49**, 508–519 (2004).
52. J. T. O. Kirk, *Light and Photosynthesis in Aquatic Ecosystems* (Cambridge Univ. Press, ed. 3, 2011), p. 199.
53. Y. Zhang, B. Kieft, B. W. Hobson, J. P. Ryan, B. Barone, C. M. Preston, B. Roman, B.-Y. Raanan, R. Marin III, T. C. O'Reilly, C. A. Rueda, D. Pargett, K. M. Yamahara, S. Poulos, A. Romano, G. Foreman, H. Ramm, S. T. Wilson, E. F. DeLong, D. M. Karl, J. M. Birch, J. G. Bellingham, C. A. Scholin, Autonomous tracking and sampling of the deep chlorophyll maximum layer in an open-ocean eddy by a long-range autonomous underwater vehicle. *IEEE J. Ocean. Eng.* **45**, 1308–1321 (2020).
54. D. M. Pargett, J. M. Birch, C. M. Preston, J. P. Ryan, Y. Zhang, C. A. Scholin, Development of a mobile ecogenomic sensor, in *OCEANS 2015 - MTS/IEEE Washington* (IEEE, 2015), pp. 1–6.
55. J. G. Bellingham, Y. Zhang, J. E. Kerwin, J. Erikson, B. Hobson, B. Kieft, M. Godin, R. McEwen, T. Hoover, J. Paul, A. Hamilton, J. Franklin, A. Banka, Efficient propulsion for the Tethys long-range autonomous underwater vehicle, in *2010 IEEE/OES Autonomous Underwater Vehicles* (IEEE, 2010), pp. 1–7.
56. K. M. Yamahara, C. M. Preston, J. Birch, K. Walz, R. Marin III, S. Jensen, D. Pargett, B. Roman, W. Ussler III, Y. Zhang, J. Ryan, B. Hobson, B. Kieft, B. Raanan, K. D. Goodwin, F. P. Chavez, C. Scholin, *In situ* autonomous acquisition and preservation of marine environmental DNA using an autonomous underwater vehicle. *Front. Mar. Sci.* **6**, 373 (2019).
57. M. J. Stanway, B. Kieft, T. Hoover, B. Hobson, A. Hamilton, J. Bellngham, Acoustic tracking and homing with a long-range AUV, in *2014 Oceans—St. John's* (IEEE, 2014), pp. 1–7.
58. T. C. O'Reilly, B. Kieft, M. Chaffey, Communications relay and autonomous tracking applications for Wave Glider, in *OCEANS 2015—Genova* (IEEE, 2015), pp. 1–6.
59. J. Birch, B. Barone, E. DeLong, G. Foreman, K. Gomes, B. Hobson, S. Jensen, D. Karl, B. Kieft, R. Marin III, T. O'Reilly, D. Pargett, C. Preston, B. Roman, A. Romano, J. Ryan, C. Scholin, W. Ussler, K. Yamahara, Y. Zhang, Autonomous targeted sampling of the deep chlorophyll maximum layer in a subtropical North Pacific eddy, in *OCEANS 2018 MTS/IEEE Charleston* (IEEE, 2018), pp. 1–5.
60. B. Barone, *Characteristics and Mechanisms of Formation of a Chlorophyll Maximum in a Subtropical Gyre* (Università degli Studi di Napoli Federico II, 2009).
61. L. D. Talley, G. L. Pickard, W. J. Emery, J. H. Swift, *Descriptive Physical Oceanography: An Introduction* (Academic Press, ed. 6, 2011), pp. 200–203.
62. R. J. Olson, H. M. Sosik, A submersible imaging-in-flow instrument to analyze nano- and microplankton: Imaging FlowCytobot. *Limnol. Oceanogr. Methods* **5**, 195–203 (2007).
63. E. L. Venrick, Phytoplankton in an oligotrophic ocean: Species structure and interannual variability. *Ecology* **71**, 1547–1563 (1990).
64. S. Imbeaud, E. Graudens, V. Boulanger, X. Barlet, P. Zaborski, E. Eveno, O. Mueller, A. Schroeder, C. Auffray, Towards standardization of RNA quality assessment using user-independent classifiers of microcapillary electrophoresis traces. *Nucleic Acids Res.* **33**, e56 (2005).
65. D. M. Karl, R. R. Bidigare, R. M. Letelier, Sustained and aperiodic variability in organic matter production and phototrophic microbial community structure in the North Pacific subtropical gyre, in *Phytoplankton Productivity: Carbon Assimilation in Marine and Freshwater Ecosystems*, P. J. le B. Williams, D. N. Thomas, C. S. Reynolds, Eds. (Wiley, 2002), pp. 222–264.
66. K. Fennel, E. Boss, Subsurface maxima of phytoplankton and chlorophyll: Steady-state solutions from a simple model. *Limnol. Oceanogr.* **48**, 1521–1534 (2003).
67. D. A. Siegel, T. D. Dickey, L. Washburn, M. K. Hamilton, B. G. Mitchell, Optical determination of particulate abundance and production variations in the oligotrophic ocean. *Deep Sea Res. Part I Oceanogr. Res. Pap.* **36**, 211–222 (1989).
68. J. P. Ryan, R. M. Kudela, J. M. Birch, M. Blum, H. A. Bowers, F. P. Chavez, G. J. Doucette, R. Marin III, C. M. Mikulski, J. T. Pennington, C. A. Scholin, G. J. Smith, A. Woods, Y. Zhang, Causality of an extreme harmful algal bloom in Monterey Bay, California, during the 2014-2016 northeast Pacific warm anomaly. *Geophys. Res. Lett.* **44**, 5571–5579 (2017).
69. W. Ussler, C. Preston, L. Lingerfelt, C. Mikulski, P. Den Uyl, T. Johengen, A. Vander Woude, R. Errera, S. Ruberg, K. Goodwin, B. Kieft, B. Hobson, J. Birch, C. Scholin, G. Doucette, The 3rd generation ESP/long-range AUV: First tests of autonomous, underway sampling and analysis of microcystin in western Lake Erie, in *10th US Symposium on Harmful Algae* (U.S. National Office for Harmful Algal Blooms, 2019).
70. J. G. Bellingham, T. R. Consi, State configured layered control, in *Proceedings of IARP 1st Workshop on Mobile Robots for Subsea* (International Advanced Robotics Programme, 1990).
71. M. A. Godin, J. G. Bellingham, B. Kieft, R. McEwen, Scripting language for state configured layered control of the Tethys long range autonomous underwater vehicle, in *OCEANS 2010 MTS/IEEE SEATTLE* (IEEE, 2010), pp. 1–7.
72. R. M. Letelier, R. R. Bidigare, D. V. Hebel, M. Ondrusek, C. D. Winn, D. M. Karl, Temporal variability of phytoplankton community structure based on pigment analysis. *Limnol. Oceanogr.* **38**, 1420–1437 (1993).
73. Y. Zhang, B. Kieft, B. W. Hobson, B.-Y. Raanan, S. S. Urmy, K. J. Pitz, C. M. Preston, B. Roman, K. J. Benoit-Bird, J. M. Birch, F. P. Chavez, C. A. Scholin, Persistent sampling of vertically migrating biological layers by an autonomous underwater vehicle within the beam of a seabed-mounted echosounder. *IEEE J. Ocean. Eng.*, (2020).
74. J. T. McClave, T. Sincich, *Statistics* (Pearson Education Inc., ed. 13, 2017), pp. 433–464.
75. B. Barone, R. R. Bidigare, M. J. Church, D. M. Karl, R. M. Letelier, A. E. White, Particle distributions and dynamics in the euphotic zone of the North Pacific Subtropical Gyre. *J. Geophys. Res. Oceans* **120**, 3229–3247 (2015).
76. A. E. White, B. Barone, R. M. Letelier, D. M. Karl, Productivity diagnosed from the diel cycle of particulate carbon in the North Pacific Subtropical Gyre. *Geophys. Res. Lett.* **44**, 3752–3760 (2017).

Downloaded from http://robotics.sciencemag.org/ at MLML MBARI on January 13, 2021

Acknowledgments: We are thankful to the Schmidt Ocean Institute and R/V *Falkor* Captain and crew for their technical assistance and public outreach support. Before his untimely passing, R. Marin III contributed to the development of the 3G-ESP and played a leading role in the field experiment reported herein; he is dearly missed by his colleagues. G. Foreman participated in the LRAUV operations. T. O'Reilly and H. Ramm monitored the Wave Glider operation. P. Den Uyl assisted with post-deployment 3G-ESP controls, recovery of 3G-ESP samples, and the collection of shipboard CTD rosette samples. R. Tabata, T. Burrell, E. Shimabukuro, and T. Clemente deployed the underway CTD during the initial eddy survey. E. Shimabukuro collected and analyzed samples for conventional flow cytometry. E. Firing and J. Hummon processed the shipboard ADCP data, and L. Fujieki provided access to the processed ADCP data. M. Godin, R. McEwen, M. J. Stanway, J. Erickson, M. Chaffey, E. Mellinger, D. Klimov, and T. Hoover contributed to the LRAUV development. W. Ussler, S. Jensen, and K. Yamahara contributed to the 3G-ESP development. M. Godin and C. Rueda developed the LRAUV operation portal, and K. Gomes managed the MBARI ODSS (Oceanographic Decision Support System). B. Watkins, E. Wood-Charlson, and T. Hoffman provided operational and logistical support. M. Salisbury did graphical work for Figs. 2 and 5. The time-series data from Station ALOHA used to produce Fig. 1 came from the Hawaii Ocean Time-series Data Organization and Graphical System (http://hahana.soest.hawaii.edu/hot/hot-dogs/interface.html). The SLA and geostrophic current velocity data came from the Copernicus Marine Environment Monitoring Service (CMEMS; http://marine.copernicus.eu/). This work is a contribution of the SCOPE and the Center for Microbial Oceanography: Research and Education. **Funding:** This work was supported by the NSF (OCE-0962032 to C.A.S. and J.M.B., and OCE-1337601 to C.A.S., J.G.B., B.W.H., and J.M.B.), the Simons Foundation (grant 329108 to D.M.K., E.F.D., and A.E.W.), the Gordon and Betty Moore Foundation (grant 3794 to D.M.K.; grant 3777 to E.F.D.; grant 2728 to C.A.S.), NSF OCE-1756517 (for Hawaii Ocean Time-series HOT-DOGS data), the David and Lucile Packard Foundation, and the Schmidt Ocean Institute for R/V *Falkor* Cruise FK180310. **Author contributions:** C.A.S., E.F.D., D.M.K., J.M.B., B.W.H., and J.G.B. conceived the experiment. B.W.H., B.K., Y.Z., and B.-Y.R. led the LRAUV operations. Y.Z., B.K., B.B., and J.P.R. developed the LRAUV algorithms. C.M.P., B.R., and A.R. prepared and processed the 3G-ESP cartridges. D.P. led the development of the 3G-ESP. S.P. and S.T.W. were chief scientists of leg 1 and leg 2, respectively. A.R. completed the RNA extraction, quantification, and quality analysis of the water samples acquired by the 3G-ESP and the shipboard CTD rosette. M.D. and A.E.W. operated the IFCB and processed the images. A.E.W. and F.H.F. processed the shipboard CTD rosette chlorophyll fluorescence and optical beam attenuation data. F.H.F. processed the real-time SLA and shipboard ADCP data. Y.Z. and J.P.R. led data analysis, manuscript drafting, and revision, incorporating all input from coauthors and reviewers. **Competing interests:** The authors declare that they have no competing financial interests. **Data and materials availability:** All data needed to evaluate the conclusions are presented in the paper or the Supplementary Materials.

Submitted 6 May 2020
Accepted 14 December 2020
Published 13 January 2021
10.1126/scirobotics.abb9138

Citation: Y. Zhang, J. P. Ryan, B. W. Hobson, B. Kieft, A. Romano, B. Barone, C. M. Preston, B. Roman, B.-Y. Raanan, D. Pargett, M. Dugenne, A. E. White, F. Henderikx Freitas, S. Poulos, S. T. Wilson, E. F. DeLong, D. M. Karl, J. M. Birch, J. G. Bellingham, C. A. Scholin, A system of coordinated autonomous robots for Lagrangian studies of microbes in the oceanic deep chlorophyll maximum. *Sci. Robot.* **6**, eabb9138 (2021).

Downloaded from http://robotics.sciencemag.org/ at MLML MBARI on January 13, 2021

Science Robotics

A system of coordinated autonomous robots for Lagrangian studies of microbes in the oceanic deep chlorophyll maximum

Yanwu Zhang, John P. Ryan, Brett W. Hobson, Brian Kieft, Anna Romano, Benedetto Barone, Christina M. Preston, Brent Roman, Ben-Yair Raanan, Douglas Pargett, Mathilde Dugenne, Angelicque E. White, Fernanda Henderikx Freitas, Steve Poulos, Samuel T. Wilson, Edward F. DeLong, David M. Karl, James M. Birch, James G. Bellingham and Christopher A. Scholin

Sci. Robotics **6**, eabb9138.
DOI: 10.1126/scirobotics.abb9138

ARTICLE TOOLS http://robotics.sciencemag.org/content/6/50/eabb9138

SUPPLEMENTARY MATERIALS http://robotics.sciencemag.org/content/suppl/2021/01/11/6.50.eabb9138.DC1

RELATED CONTENT http://robotics.sciencemag.org/content/robotics/6/50/eabf4317.full
http://robotics.sciencemag.org/content/robotics/4/27/eaav3041.full

REFERENCES This article cites 52 articles, 9 of which you can access for free
http://robotics.sciencemag.org/content/6/50/eabb9138#BIBL

PERMISSIONS http://www.sciencemag.org/help/reprints-and-permissions

Use of this article is subject to the Terms of Service

Science Robotics (ISSN 2470-9476) is published by the American Association for the Advancement of Science, 1200 New York Avenue NW, Washington, DC 20005. The title *Science Robotics* is a registered trademark of AAAS.

Copyright © 2021 The Authors, some rights reserved; exclusive licensee American Association for the Advancement of Science. No claim to original U.S. Government Works

Downloaded from http://robotics.sciencemag.org/ at MLML MBARI on January 13, 2021

Science Robotics
AAAS

robotics.sciencemag.org/cgi/content/full/6/50/eabb9138/DC1

Supplementary Materials for

A system of coordinated autonomous robots for Lagrangian studies of microbes in the oceanic deep chlorophyll maximum

Yanwu Zhang*, John P. Ryan, Brett W. Hobson, Brian Kieft, Anna Romano, Benedetto Barone, Christina M. Preston, Brent Roman, Ben-Yair Raanan, Douglas Pargett, Mathilde Dugenne, Angelicque E. White, Fernanda Henderikx Freitas, Steve Poulos, Samuel T. Wilson, Edward F. DeLong, David M. Karl, James M. Birch, James G. Bellingham, Christopher A. Scholin

*Corresponding author. Email: yzhang@mbari.org

Published 13 January 2021, *Sci. Robot.* **6**, eabb9138 (2021)
DOI: 10.1126/scirobotics.abb9138

This PDF file includes:

Section S1. Method for computing average profiles of physical, chemical, and bio-optical conditions at Station ALOHA.
Section S2. Method for computing statistical summaries from profiles of chloropigment and particulate beam attenuation coefficient from shipboard CTD rosette measurements.
Section S3. Methods for ship-based current velocity measurement and comparison with drift velocities.
Section S4. Methods for shipboard sampling for RNA analysis.
Section S5. Methods for RNA extraction from shipboard and ESP samples.
Section S6. Methods for shipboard sampling for conventional and imaging flow cytometry and statistical analysis.
Section S7. Methods for sea-surface PAR measurement and statistical analysis.
Fig. S1. Ship-based characterization of the DCM.
Fig. S2. Lagrangian drift velocities.
Fig. S3. Vertical variation of horizontal current speed.
Fig. S4. Water-column biomass characterization.
Fig. S5. Localization of the DCM followed by Lagrangian drift within the DCM.
References (*75*, *76*)

Method for computing average profiles of physical, chemical, and bio-optical conditions at Station ALOHA

To represent the typical structure of the DCM and the underlying distributions of density, photosynthetic pigments, nutrients, and light in the water column of the study region (Figure 1A), we computed climatological average profiles from the Hawaii Ocean Time-series (HOT) observations at Station ALOHA (22°45'N, 158°W; Figure 1B). All analyses were constrained to March-April, the months of our study. The average profiles of potential density anomaly, chloropigment (chlorophylls+phaeopigments), and nitrate+nitrite concentrations were computed from measurements from March 1990 to April 2018; the average photosynthetically active radiation (PAR) profile was computed from measurements from March 1998 to April 2009.

Method for computing statistical summaries from profiles of chloropigment and particulate beam attenuation coefficient from shipboard CTD rosette measurements

To evaluate whether the DCM coincided with a local maximum in particle concentrations in the water column within the cyclonic eddy, we examined profiles of calibrated measurements of chloropigment (chlorophylls+phaeopigments [66]) and optical beam attenuation [75] [76] measured respectively by the fluorometer and the transmissometer installed on the shipboard CTD rosette. Beam attenuation coefficient was averaged within the depth range 380 to 400 m, then subtracted from the profile to represent particulate beam attenuation coefficient (c_p) within the overlying water column. For each leg (16 profiles from leg 1; 37 profiles from leg 2), the mean and standard deviation (sd) of c_p were computed within isopycnal layers using data from the upper 200 m, represented as the mean profile with a 1 sd envelope (Figure S1).

Methods for ship-based current velocity measurement and comparison with drift velocities

An OS75 Acoustic Doppler Current Profiler (ADCP) (Teledyne RD Instruments, Poway, CA) was installed on R/V *Falkor*. The ADCP operated at 75 kHz and measured current velocity between ~24 and 500 m depths in 8-m bins. The ADCP data were logged at 5-minute intervals. Earth-referenced current velocity was derived from the water velocity relative to the ADCP, and the ship (ADCP) velocity relative to the Earth (from GPS position). Velocity data from the ADCP were used for two purposes. The first was to compare the velocity of the drifting *Aku* with ADCP-measured current velocity at the depth of *Aku*. Because the eddy created substantial velocity gradients (Figure 3A), this comparison was constrained to ADCP velocity measurements within 5 km of *Aku*. Sufficient data for comparison were acquired during three periods of each sampling leg (Figure S2). The Wilcoxon rank-sum test showed that speed estimates from matched segments of ship ADCP measurements and *Aku* drift trajectory (Figure S2) were equivalent (median speeds of 0.24 and 0.25 m/s, respectively; $p = 0.48$). Bartlett's test of homogeneity of variances did not reject the null hypothesis of equal variances (standard deviations of 0.05 m/s for both platforms; $p = 0.97$), therefore Student's t-test was the appropriate parametric test for equivalence of means. The t-test did not reject the null hypothesis of equivalence of means (0.22 and 0.25 m/s, respectively; $p = 0.42$). The second purpose was to examine the current speed profile from near-surface to the 120-m drogue depth of the drifter (Figure S3), using ADCP velocity measurements acquired within 5 km of the drifter.

Methods for shipboard sampling for RNA analysis

The CTD rosette carried a fluorometer and transmitted the real-time chlorophyll fluorescence and temperature profiles to the shipboard lab via the electro-mechanical cable. DCM sampling followed the same principle as that used by the sampling LRAUV. At the first CTD rosette sampling station of each leg, the scientists visually inspected the profiles and determined the isotherm that corresponded to the

DCM chlorophyll peak. At successive sampling stations of each leg, a Niskin bottle was manually triggered at the depth of the targeted isotherm to acquire the DCM water sample.

Shipboard samples for RNA analysis were collected at 50-m depth, DCM, and 250-m depth using the CTD rosette deployed at 06:00, 12:00, and 18:00 HST (Hawaii Standard Time) for 18 time points per leg. Seawater collected in Niskin bottles was filtered to collect and estimate particulate RNA transcripts. Two liters of seawater per depth were filtered through stacked 5 μm and 0.22 μm filters (the same pore sizes as those of the ESP filters) housed in a Swinnex filter holder (MilliporeSigma, Burlington, MA), that was attached to Masterflex tubing L/S 15 (Cole Parmer, Vernon Hills, IL) fed through a peristaltic single channel head. The peristaltic pump speed was set to 80 mL/minute. Duplicate filters were collected per time point and depth. Filters were removed from the Swinnex holder using ethanol cleaned forceps and placed in polymerase chain reaction (PCR) clean 2.0 mL tubes with 0.3 mL RNAlater. Filters were coated with RNAlater and left for approximately 10 minutes prior to storing at -80˚C. Filtration volumes were measured with a 2 L graduated cylinder.

Methods for RNA extraction from shipboard and ESP samples

The 0.22 μm filters from ship and ESP sampling were stored on ice upon removal from -80°C storage. The samples were centrifuged at 2000 rcf for 30 seconds prior to removal of RNAlater. A total of 300 μL of denaturing solution lysis buffer (Ambion, Inc., Austin, TX) was added to each filter, vortexed for 1 minute, and then stored on ice. Next, to target 1% of total sample reads, 2 μL of diluted (1/100) ERCC "spike in" RNA standards (ThermoFisher Scientific, Hampton, NH) were added to the lysate prior to purification with 898 μL of nuclease free water (Ambion, Inc.). RNA purification was performed using the Magnetic Separation Module (MSM) instrument with a 96-rod head (PerkinElmer, Waltham, MA). Into each sample well, 650 μL of sample were loaded in duplicate, and the instrument was loaded with MSM reagents from Tissue RNA kit (CMG-1212, PerkinElmer), and 80 μL DNA free magnetic beads were added to each sample well. Samples were DNase treated on board the instrument during the purification protocol. After magnetic bead purification, samples were eluted with 50 μL of RNase free water. RNA eluates were spilt into two plates and sealed for long-term storage at -80°C. A 6-μL aliquot (stored at -80°C) was reserved for RNA quality and quantification tests.

Methods for shipboard sampling for conventional and imaging flow cytometry and statistical analysis

Estimates of phytoplankton cell concentration across the water column were made by coupling conventional (Influx Cell Sorter flow cytometer, BD Biosciences, San Jose, CA) and imaging flow cytometry (IFCB, McLane Research and Laboratories, Inc., East Falmouth, MA). The two instruments offer complementary data sets comprising cell counts and optical fingerprints of photosynthetic picoeukaryotes (PPEs) in the size range 0.8-3 μm and larger phytoplankton (4-100 μm) respectively.

For conventional flow cytometry, shipboard samples were collected at HOT standard depths (5, 25, 45, 75, 100, 125, 150, 175 m) using the CTD rosette deployed at 02:00, 04:00, 16:00, and 22:00 HST for legs 1 and 2. One-mL samples were fixed with paraformaldehyde (0.2 μm syringe filtered; 0.25% final concentration) in the dark at room temperature for 15 minutes prior to flash freezing in liquid nitrogen and stored at -80°C. Both light scattering and autofluorescence emission of cells' photopigments were recorded as individual cells passed through a 200 mW 488 nm laser. PPEs were identified based on their optical fingerprints (light scatter and fluorescence emission) and subsequently counted using the acquisition software Spigot (BD Biosciences).

For imaging flow cytometry, shipboard samples were collected at the DCM and within the mixed layer (5 and 15 m) during leg 2 only from the CTD rosette deployed at 06:00, 12:00, and 18:00 HST. Samples of 5

mL were analyzed within 3 hours after collection to acquire high resolution images used to identify phytoplankton cells and subsequently count the total cell concentration of phytoplankton larger than 4 µm. For each sample, cells (including photosynthetic and non-photosynthetic species) were manually classified at the genera level and annotated as either autotrophs or heterotrophs based on the literature.

PPE and corresponding chloropigment concentrations were examined for two purposes. The first was to evaluate whether the DCM represented a local maximum in PPE concentrations within the water column. The second was to test whether chloropigment and PPE concentrations within the DCM decreased between the first and second sampling legs. Neither variable was normally distributed (Shapiro-Wilk normality test, $p < 0.05$), thus the non-parametric two-sample Wilcoxon rank-sum test was applied to test significance of the differences.

Methods for sea-surface PAR measurement and statistical analysis

Photosynthetically active radiation (PAR) levels at the sea surface during the two DCM sampling legs were measured by a LI-1500 Light Sensor Logger (LICOR, Lincoln, NE) installed on the deck of R/V *Falkor*. The PAR data were logged at 1-minute intervals. We calculated the daily average PAR levels (from midnight to midnight) of 16-20 March for leg 1 and those of 28 March to 1 April for leg 2. The null hypothesis that the means of the daily average PAR levels during DCM sampling on legs 1 and 2 were equal was not rejected (Student's t-test, $p = 0.91$; following Levene's test, $p = 0.45$, hence the null hypothesis of equal variances was not rejected). We used software R (release 3.5.3; http://www.R-project.org/) for statistical analysis.

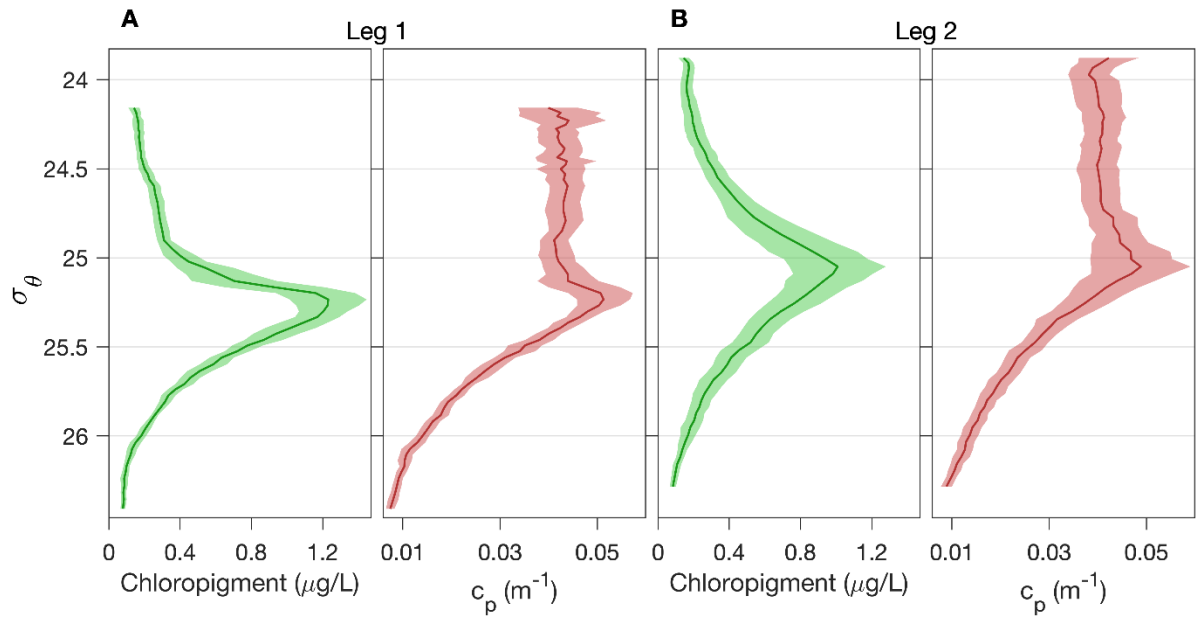

Fig. S1. Ship-based characterization of the deep chlorophyll maximum. Profiles of the mean and envelope (± one standard deviation) of chloropigment (chlorophylls + phaeopigments) and particulate beam attenuation coefficient (c_p) during sampling legs 1 (A) and 2 (B).

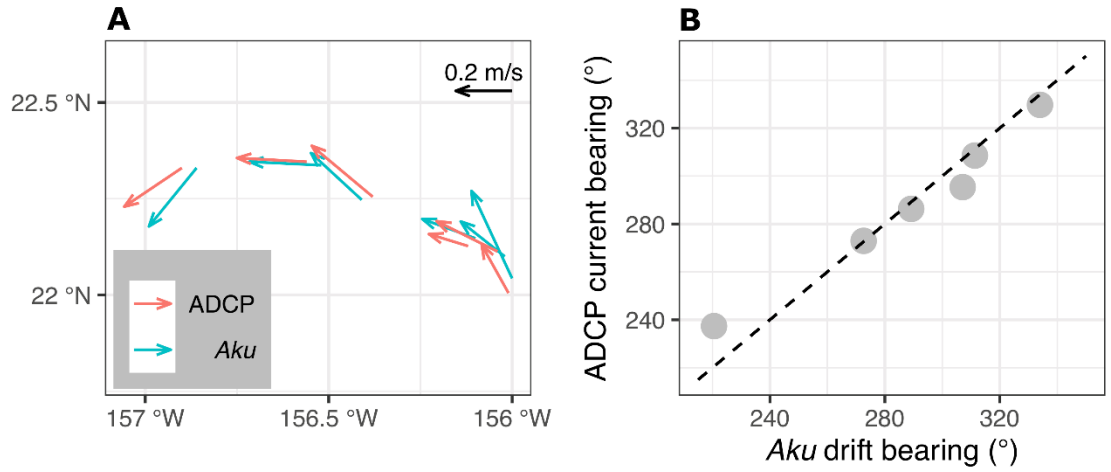

Fig. S2. Lagrangian drift velocities. (A) *Aku* drift velocity compared with nearby (3.9 ± 0.8 km in leg 1 and 3.7 ± 0.9 km in leg 2) Earth-referenced horizontal current velocity measured by R/V *Falkor* shipboard Acoustic Doppler Current Profiler at the depth of *Aku* in sampling leg 1 (east of 156.25ºW) and leg 2 (west of 156.25ºW). (B) Scatter plot of the bearings of each pair of velocity vectors in (A). The 1:1 dashed line is shown for reference.

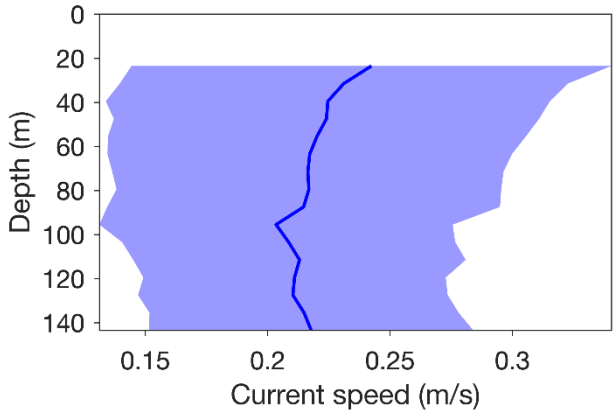

Fig. S3. Vertical variation of horizontal current speed. Profile of the mean and envelope (± one standard deviation) of Earth-referenced horizontal current speed (measured by R/V *Falkor* shipboard Acoustic Doppler Current Profiler) averaged over locations near the drogued drifter (3.1 ± 1.1 km in leg 1 and 3.2 ± 1.1 km in leg 2).

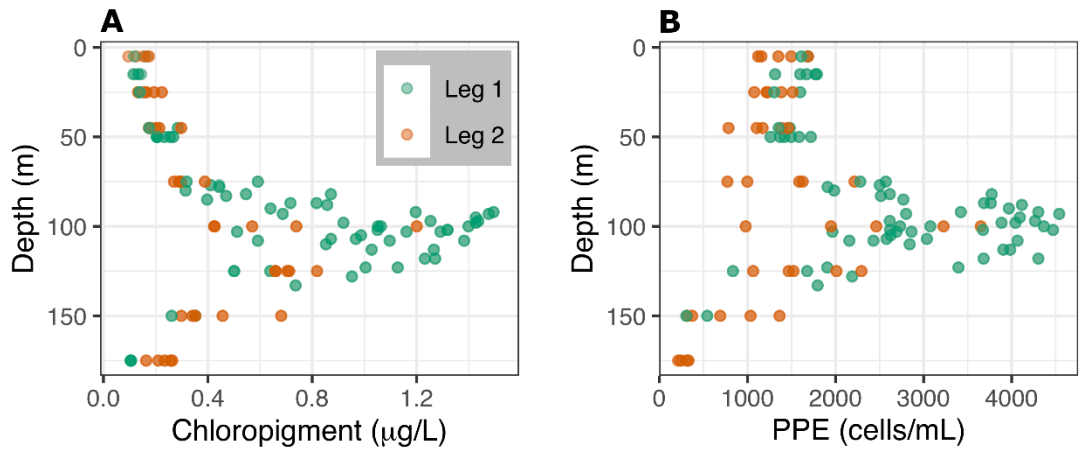

Fig. S4. Water-column biomass characterization. Concentrations of (A) chloropigment (chlorophylls + phaeopigments) and (B) photosynthetic picoeukaryotes (PPEs) from ship conductivity-temperature-depth rosette samples in legs 1 and 2.

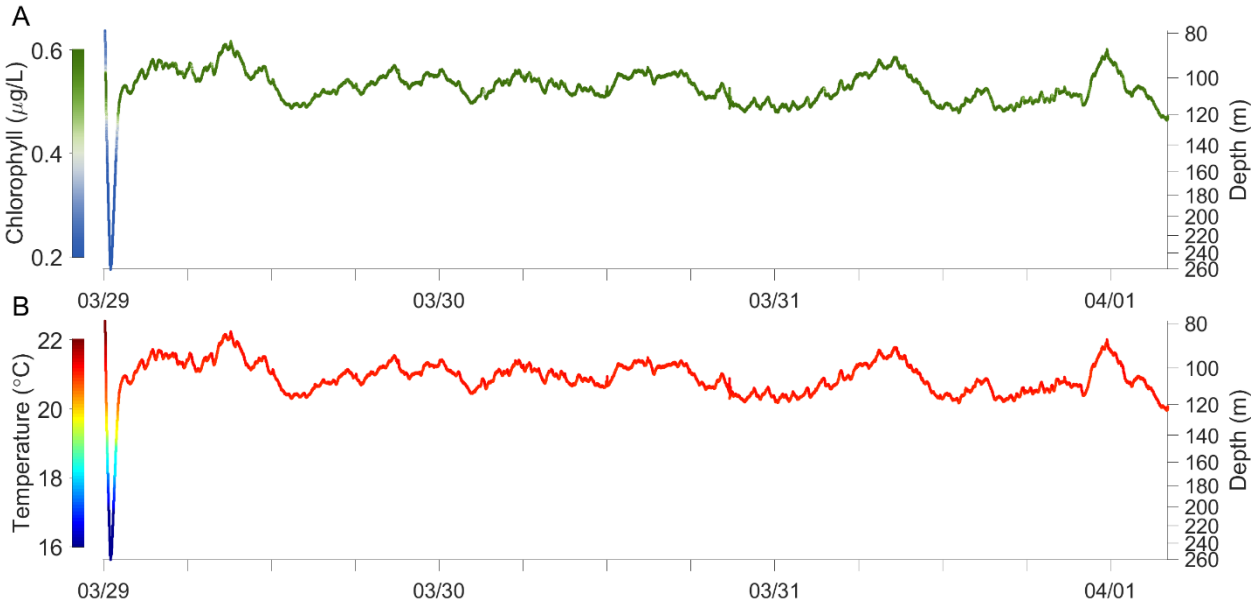

Fig. S5. Localization of the deep chlorophyll maximum (DCM) followed by Lagrangian drift within the DCM. Fluorescence-derived chlorophyll (A) and temperature (B) measured by *Aku* during leg 2. *Aku* descended from the surface to 260-m depth to find the peak of the chlorophyll signal in the water column and the corresponding temperature. It then ascended to reach the recorded chlorophyll-peak associated temperature, and thereafter actively adjusted its depth to remain at that temperature so as to track the DCM (Figure 4). Time is UTC.